Chemical Engineering Journal 328 (2017) 717–736

Contents lists available at ScienceDirect

Chemical Engineering Journal

journal homepage: www.elsevier.com/locate/cej

Experimental and numerical hydrodynamic studies of ionic liquid-aqueous plug flow in small channels

Qi Li, Panagiota Angeli *

Department of Chemical Engineering, University College London, Torrington Place, London WC1E 7JE, UK

HIGHLIGHTS

- Detailed plug flow characteristics in liquid-liquid microchannel flows.
- Velocity profiles and circulation patterns in plugs were obtained with bright field PIV.
- CFD simulations predicted well experimental plug lengths.
- Variation of pressure along the microchannel during plug flow.

ARTICLE INFO

Article history:
Received 31 March 2017
Received in revised form 1 July 2017
Accepted 6 July 2017
Available online 8 July 2017

Keywords:
Liquid-liquid
Plug flow
PIV, CFD
Microchannels

ABSTRACT

The hydrodynamic characteristics of liquid-liquid plug flow were studied in microchannels with 0.2 and 0.5 mm ID both experimentally and numerically. For the experiments high speed imaging and bright field micro-Particle Image Velocimetry were used, while the numerical simulations were based on the volume-of-fluid (VOF) method. The two immiscible liquids were a 1 M HNO_3 aqueous solution which formed the dispersed plugs and a mixture of 0.2 M n-octyl(phenyl)-N,N-diisobutylcarbamoylmethyphosphine oxide (CMPO) and 1.2 M Tributylphosphate (TBP) in the ionic liquid 1-butyl-3-methylimidazolium bis[(trifluoromethyl)sulfonyl]amide ($[C_4min][NTf_2]$). The thickness of the film surrounding the plugs, and the plug velocity and length were measured and compared against literature correlations. For the cases studied ($0.0224 < Ca < 0.299$) it was observed that the liquid film was largely affected by the changes in the shape of the front cap of the plug. The plug length was affected by both the Capillary number and the ratio of the aqueous to ionic liquid phase flow rates while the plug volume depended on the channel diameter and the mixture velocity. The numerical simulations showed that, in agreement with the measurements, a parabolic velocity profile develops in the middle of the plugs while the circulation patterns in the plug are affected by the channel size. The pressure profile along the channel with a series of plugs and slugs was predicted numerically while the pressure drop agreed well with a correlation which included the dimensionless slug length and the ratio Ca/Re.

1. Introduction

Technical and environmental reasons are driving the development of small scale and miniaturised equipment within the frame of process intensification. The small scales reduce the molecular diffusion distances and increase the importance of surface/interfacial forces which bring new research challenges in the study of the hydrodynamic features and transport phenomena, particularly for multiphase systems [1–3]. Taylor (plug/segmented) flow in gas-liquid and liquid-liquid systems, where a continuous liquid phase separates elongated bubbles or drops (plugs) is a preferred pattern because the plug sizes are regular and can be controlled via the choice of inlet geometry. In addition, recirculation patterns establish in the liquid phases while the thin films that separate the bubbles/plugs from the channel wall enhance interphase and bubble (plug)-wall mass transfer [4–7]. Liquid-liquid microfluidic systems have found applications in solvent extraction [8–10], dispersion/emulsion formation [11], chemical synthesis/catalysis and biomedical analysis.

For the design of microfluidic devices operating in liquid-liquid plug flow, knowledge of hydrodynamic parameters such as film thickness, plug length/velocity and pressure drop is particularly important [12]. The significance of the film, which is formed due to viscous effects between the liquid plug and the wall is that the whole enclosed plug surface can participate in mass transfer.

---

* Corresponding author.
E-mail address: p.angeli@ucl.ac.uk (P. Angeli).

http://dx.doi.org/10.1016/j.cej.2017.07.037
1385-8947/

Nomenclature

Ca	Capillary number, $Ca=\frac{\mu_{IL}U_p}{\sigma}$, dimensionless
f	friction factor, dimensionless
ID	channel internal diameter, mm
L	length, m
L^*	dimensionless length, dimensionless
n	Refractive index, dimensionless
Q_{aq}	volumetric flow rate of aqueous phase, $ml\cdot h^{-1}$
Q_{IL}	volumetric flow rate of ionic liquid phase, $ml\cdot h^{-1}$
r	radius distance, m
r^0	location of recirculation centre, m
R	channel internal radius, mm
Re	Reynolds number, $Re = \frac{\rho U_{mix} ID}{\mu}$, dimensionless
R_p	plug width, m
U_f	film velocity, $m\cdot s^{-1}$
U_{mix}	mixture velocity, $m\cdot s^{-1}$
U_p	plug velocity, $m\cdot s^{-1}$
$U_{x,p}$	horizontal velocity profile in aqueous plug, $m\cdot s^{-1}$
$U_{x,f}$	horizontal velocity profile in continuous film, $m\cdot s^{-1}$
W	channel width, m
We	Weber number, $We = \frac{\rho U_{mix}^2 ID}{\sigma}$, dimensionless
ΔP	Pressure drop, Pa

Greek Symbol

α	fitting parameter, dimensionless
β	fitting parameter, dimensionless
σ	interfacial tension, $N\cdot m^{-1}$
δ	film thickness, m
ε	dispersed phase fraction, dimensionless
λ	viscosity ratio, dimensionless
μ	dynamic viscosity, cp
ρ	density, $kg\cdot m^{-3}$
φ	droplet effect parameter, $\varphi = \frac{\Delta P_p D}{\mu U_{mix}}$, dimensionless

Subscript

aq	aqueous phase
c	continuous phase
d	dispersed phase
IL	ionic liquid phase
max	maximum value
mix	mixture phase
p	plug
s	slug

The film thickness depends on a number of parameters, including interfacial tension, the viscosity ratio between the two phases, and the phase flowrates, and can vary along the length of the plug [13–16]. The length of the dispersed plugs and continuous phase slugs is also very important for heat and mass transfer processes and depends on many parameters such as fluid properties and superficial velocities, represented by dimensionless groups such as Re and Ca [6,17]. It has been shown, however, that the inlet configuration has a significant effect on the plug or slug size and attempts have been made to predict it by studying the plug formation mechanisms. In the squeezing regime ($10^{-4}<Ca < 0.002$, $L_p/W > 2.5$), when the shear forces dominate over the interfacial ones, the plug break-up process is mainly controlled by the pressure drop across the plug, and the plug size is determined solely by the volumetric flow rate ratio of the two immiscible fluids [18]. In the dripping regime ($0.01 < Ca < 0.3$, $L_p/W < 1$), the formation process is dominated by both the shear and the interfacial forces, and the size depends on the Capillary number only [19,20]. In the transition regime ($0.002 < Ca < 0.01$, $1 < L_p/W < 2.5$), the plug size depends on all these forces [21].

Apart from the geometric characteristics of the plug, pressure drop in plug flows is important for the design of the pumps and for the choice of the flowrates while it can even affect the operation of the separation units at the channel outlet. In multiphase flows, the presence of the interfaces contributes an additional Laplace pressure term to the frictional component. The total pressure drop can then be calculated as a sum of the pressure drop due to the interfaces and of the frictional pressure drop of the various parts of the plug flow, i.e. film, slug and plug [12,22,23]. In these models it is assumed that the film is uniform along the plug. In simplified approaches, the overall pressure drop can also be calculated by adding in the continuous single phase pressure drop a term which accounts for the presence of the second phase [24–26].

The hydrodynamics of liquid-liquid plug flow in microchannels have been studied numerically with Computational Fluid Dynamics (CFD) simulations by a number of investigators. Different aspects of plug flow were considered, such as plug formation at the inlet [27,28], film thickness [12], velocity profiles and circulation inside the plugs [29], and pressure drop [23,30]. These studies have used either a fixed reference frame when plug formation is considered at the inlet or a moving one and periodic conditions when an isolated plug is investigated [31]. Kurup and Basu [32] compared simulated and experimental velocity profiles obtained with micro-Particle Image Velocimetry (μPIV) and found that the circulation patterns largely depend on the Capillary number. The simulated recirculation times, defined as the average time to displace material from one to the other end of the plug/slug, were found to be affected by a number of factors such as flow velocity, plug length, channel size, and viscosity ratio between the two phases [7,33,34].

To improve the understanding of liquid-liquid microchannel plug flows and to validate the numerical predictions detailed velocity measurements are needed. Non-intrusive optical techniques, such as micro-Particle Image Velocimetry, can extract multipoint information in velocity fields with high accuracy and spatio-temporal resolution. Few studies are available with μPIV in liquid-liquid microchannel flows which explore the plug formation process [35] and the local mixing inside the plugs or slugs [36,37]. In common μPIV approaches, laser light is used to volume illuminate the microchannels and the plane of measurement is defined by the focus of the camera; for temporally resolved measurements high speed lasers or a combination of continuous lasers with high speed cameras are required. A simpler approach, which does not require the use of lasers, is bright field (micro) PIV, where white light is used to illuminate the microchannel and the shadows of the tracing particles are captured by camera. For temporally resolved measurements high speed cameras can be used.

The improved heat and mass transfer rates in microscale units increase efficiencies and can reduce the overall solvent volumes required in two-phase processes such as liquid-liquid extractions. This enables novel and sometimes expensive solvents, such as ionic liquids, to be used economically. We have shown in previous work that the use of ionic liquids in small channel extraction units can enhance significantly mass transfer [10,38]. In particular, mass transfer coefficients as high as $0.05\ s^{-1}$ were found during the extraction of Eu(III) from nitric acid solutions into an ionic liquid mixture (CMPO/TBP/[C_4min][NTf_2]) in microchannels operating in plug flow. In the current paper, the detailed hydrodynamics of the plug flow regime for the same liquid-liquid system are studied systematically using bright field μPIV. The velocity fields and circulation patterns are compared against Computational Fluid Dynamics simulations in two channels with 0.2 and 0.5 mm ID. Correlations for the film thickness and plug velocity and length are also developed based on dimensionless parameters and compared against literature models.

2. Materials and experimental methodology

In the current work, a mixture of ionic liquid with CMPO and TBP (0.2 M CMPO-1.2 M TBP/[C_4min][NTf_2]) was chosen as the non-aqueous phase, while a 1 M nitric acid solution was the aqueous phase. The ionic liquid [C_4min][NTf_2], acting as diluent in the Eu(III) recovery, was obtained from the QUILL Research Centre, Queen's University of Belfast. The tri-n-butylphosphate (TBP), which acts as a modifier to prevent the formation of 'crud-type' precipitate [39], was purchased from Sigma-Aldrich. The n—octyl (phenyl)-N,N-diisobutylcarbamoylmethyphosphine oxide (CMPO) was used as extractant and was obtained from Carbosynth Limited, UK. For the preparation of the ionic liquid phase, the required amount of CMPO was added into TBP first and the mixture was mechanically shaken for 2 h. Then the mixture was introduced into the ionic liquid and stirred. Standard nitric acid solution obtained from Sigma-Aldrich was used as the aqueous phase. The aqueous phase has viscosity 0.75 cp and density 1030 kg/m^3, measured with a digital DV-III Ultra Rheometer (Brookfield, UK) and a DMA 5000 density meter (Anton Paar, UK), respectively. The viscosity and density of the ionic liquid mixture is 25.59 cp and 1259 kg/m^3, respectively. The interfacial tension of the aqueous-ionic liquid system is 6.70 mN/m, measured with a DSA 100 drop analyser (Kruss GmbH, Germany). The refractive index was measured using an Abbe 5 Refractometer (Bellingham and Stanley, UK).

The experimental set up used for the hydrodynamic studies in the microchannel is depicted in Fig. 1. Two Kds Legato syringe pumps (KD Scientific Inc., USA) were used to introduce the two liquid phases separately into the test section with a flow rate error of less than 1%. The test channel is made by quartz (Dolomite Centre Ltd, UK) and has a T-junction inlet with branches at the same diameter as the main channel. The channels have a cross section of either 0.2 or 0.5 mm internal diameter (ID). A schematic of the test section for the 0.2mm ID chip is shown in Fig. 2. Measurements were carried out at 30 mm downstream the inlet before the first bend (shown with the box in Fig. 2). To ensure consistency, in all cases studied the aqueous phase was introduced from the side channel of the T-junction and the ionic liquid phase was introduced from the side that has the same direction as the test section. For the conditions studied, the ionic liquid always became the continuous phase irrespective of the phase that initially filled the channel.

Experiments were conducted for total volumetric flow rate Q_{mix} varying from 0.653 to 35.34 ml/hr, with flow rate ratios (defined as the flow rate of the aqueous phase over the flow rate of the ionic liquid phase) varying from 0.5 to 2. These flow rates resulted in plug flow with the aqueous phase forming the dispersed plugs and the ionic liquid phase forming the continuous phase surrounding them. After each set of experiments, the microchannel was repeatedly cleaned with dichloromethane, acetone, and compressed air. Details of the cleaning process have been discussed in detail previously [10].

2.1. Plug geometric characteristics and velocity field measurements

The velocity fields inside the aqueous plugs and the hydrodynamic characteristics of the pattern, such as film thickness and plug length, were investigated with bright field micro-Particle Image Velocimetry. The test section was volumetrically illuminated with a 60 Watt continuous arc lamp, with a diffuser plane added between the backlight and the test section to minimize reflections. The interface between the two immiscible fluids appeared as a shadow under this background illumination and was captured by a high speed camera (Photron Fastcam-Ultima APX; 1024 × 1024 pixels) at frequencies adjusted between 2000 to 8000 Hz depending on the flow rates. To increase magnification, the camera was coupled with an air-immersion, long focal distance microscope lens (Leica monozoom 7) and an amplifier with magnification M = 18.9 (NA = 0.42).

For the velocity measurements, 3 μm red dyed polystyrene microspheres (Thermo Scientific; Firefili Fluorescent Red) were added as tracers in the aqueous phase, and the shadow of these

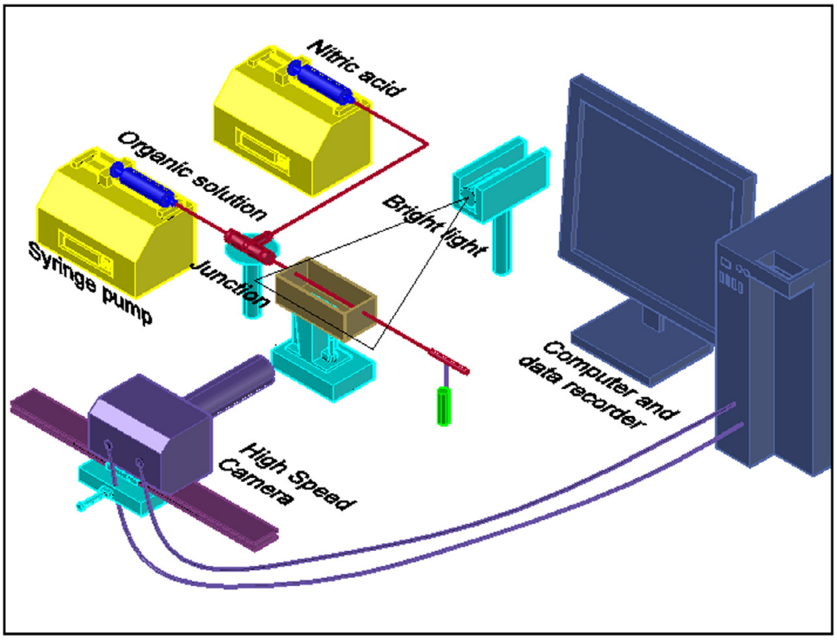

Fig. 1. Schematic of the experimental set up including the high speed micro-PIV system.

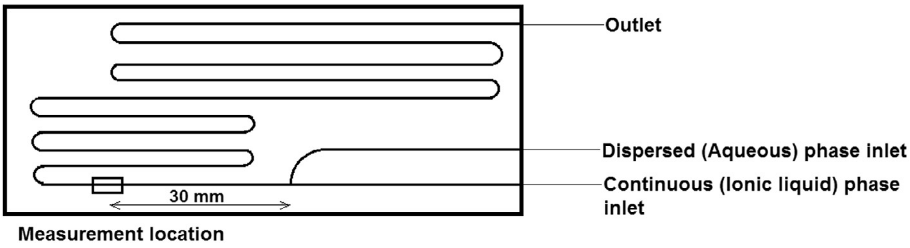

Fig. 2. Top view sketch of the 0.2 mm ID microchannel.

particles was captured on a white background in the raw pictures. With the current configuration, the field of view diameter is 0.63 mm while the depth of field [40] is given by:

$$\delta_z = \frac{3n\lambda}{NA^2} + \frac{2.16d_p}{\tan\theta} + d_p \tag{1}$$

where n is the refractive index of the immersion medium between the microfluidic device and the objective lens (air), λ is the light wavelength in vacuum (474 nm based on the arc lamp output profile), NA is the numerical aperture of the objective lens, d_p is the diameter of the PIV tracer particles and θ is the small light collection angle. For the present experiment, Eq. (1) yields δ_z around 16 μm.

Velocity field calculations between image pairs were processed with the Insight 4G Software (TSI Instruments). At first, the grayscale values of the raw images were inversed as the software requires bright particle signals on a black background [35,41]. Then a median filter was applied to the images to eliminate any background noise. The images were further normalized with a minimum intensity mask to improve the velocity field computation, which yields high particle-to-background contrast signal. The displacement of tracer particles between two consecutive frames was calculated using a square domain discretization of 32 × 32 pixels with 50% overlap to satisfy the Nyquist sampling criterion [42], which gives velocity spatial resolution of 26.72 μm × 26.72 μm in the 0.5 mm channel. The FFT correlation was used for correlation calculation while the correlation peak position was detected with a Gaussian curve by fitting the highest intensity pixel and its four nearest neighbours. The computed velocity vectors were evaluated based on three criteria: the median test as mentioned above, peak to noise ratio of 1.50, and the six-sigma validation [43]. The rejected vectors were replaced with the median value of neighbouring velocity vectors. A post-processing routine was developed in MATLAB to calculate the ensemble average of about 30 images of the instantaneous velocity vectors. For the averaging, the velocity profiles at different locations were repositioned using the plug tip location as a reference. The plug tip position was determined from the sudden change of the standard deviation of the greyscale profile across the axis of the plug. The location of the plug tip was determined with an error of ±20 pixels (±52 μm).

To obtain the plug geometric parameters for each set of flow rates about 30 plugs were averaged, with deviation between 4.25–7.10% for film thickness and 5.33–9.52% for plug length. The plug shape was determined by the clear black line between the two phases in the grayscale inversed images. Sample bright field images and their corresponding detected interface are presented in Fig. 3. Then the film thickness was obtained by subtracting the width of the aqueous plug from the channel internal diameter and dividing by 2. The plug velocity was calculated by measuring the displacement of the plug tip between two successive high speed images. Over 30 image pairs were used to calculate average plug velocities at different conditions with a deviation of 2.25–13.71%. There were small variations in the plug velocity due to small changes in pressure in the channel during plug formation at the inlet and plug exit.

2.2. CFD simulations

A fixed, three dimensional computational domain with the same geometry as the experimental test section was used for the numerical simulations, as shown in Fig. 4(a). The entrance lengths for the continuous ionic liquid and the dispersed aqueous phases are 0.7 mm and 1.5mm in the 0.2 and the 0.5mm ID channels respectively, to ensure fully developed laminar profiles [44,45]. The test section has 44 channel diameters length and was chosen so that the plug flow could be fully developed [46]. To ensure consistency with the experiments, the computational domain is initially occupied by ionic liquid. Atmospheric pressure (101,325 Pa) is used as boundary at the test section exit instead of an outflow boundary to avoid backflow. No-slip condition is applied to all wall boundaries. For the simulations the commercial CFD software FLUENT 12.1 (ANSYS Inc.) was chosen, which employs the Volume of Fluid (VOF) method for tracking the liquid-liquid interface. The first order upwind and the Green-Gauss node based gradient calculation schemes were used for time marching of the momentum/-continuity equations and the pressure gradient calculations, respectively [31,47]. The time step is controlled by a specified maximum value for the Courant number, Co = $\Delta t/(\Delta x/V)$, where Δt, Δx and V are the time step, grid size and fluid velocity respectively. A high Co value leads to an unstable numerical approach while a low Co value means very small time steps and consequently long simulation times. A maximum Co of 0.25 was adopted in this work, since the elements are very fine close to the interface and the wall, which gives time steps in the order of 10^{-7} s. The convergence criteria for velocities and pressure were set to 0.01. The absolute values of residuals achieved were found to be sufficiently low, $O(10^{-6})$ for velocities and $O(10^{-10})$ for continuity.

To correctly capture the plug formation at the microchannel inlet, the contact angle on the microchannel wall of the ionic liquid/nitric acid solution interface [28,48] needs to be specified. The equilibrium contact angle was measured by placing a nitric acid drop on the microchip surface in an ionic liquid solution environment using a DSA 100 drop analyzer (Kruss GmbH, Germany), which gave an average value of 117.54°. Using this contact angle, plug lengths for U_{mix} = 0.005 to 0.02 m/s were close to the experimental ones with an average deviation of 7.17%. However, for U_{mix} = 0.03 to 0.05 m/s, slightly higher contact angles from 122° to 131° were required to give plug lengths close to the experimental data with an average deviation ranging from 9.55 to 13.08% (see also in Li et al. [49]).

To be able to capture accurately the film thickness between the plugs and the channel wall as well as the plug breakage at the channel inlet, a very fine mesh is required. The plug shape calculated from CFD at three different grid sizes is compared in Fig. 4(b) against the experimental results for U_{mix}=0.03 m/s. As can be seen, the film thickness from the 3 μm grid size fits best the experimental results, although it slightly underpredicts the plug length by 2.03%. A symmetric grid was used as shown in Fig. 4(b). This size mesh will be used for further analysis and involves nearly 6 million hexahedron (82.84%) and tetrahedron (17.16%) type cells.

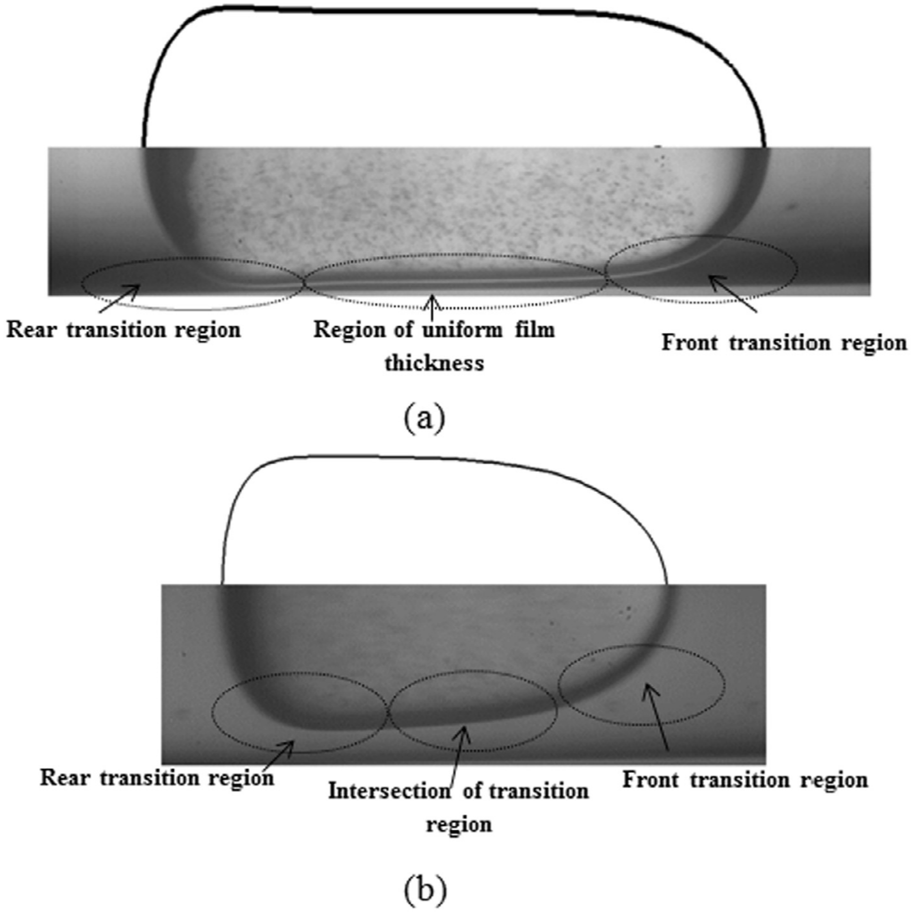

Fig. 3. Image of aqueous plugs with different dimensionless lengths (a) $L_p/D = 2.28$ and (b) $L_p/D = 1.61$in the 0.5 mm ID channel.

3. Results and discussion

The plug geometric characteristics and pressure drop are discussed in the following sections.

3.1. Film thickness

Depending on the plug length the film thickness may not be uniform along the plug (see Fig. 3). The dimensionless plug length (L_p/D) varied between 1.14 and 2.31 in both the 0.2 and 0.5 mm ID channels. It was found that for L_p/D between 1.82 and 2.31, a region of uniform film thickness was always present between the hemispherical caps of the plug and the film thickness was measured in this area. However, for $1.14 < L_p/D < 1.82$, the film thickness varied along the plug length. In these cases the film thickness was obtained by averaging the thickness at 5 points along the plug.

Because the refractive indexes of the channel wall (n = 1.544), the ionic liquid phase (n = 1.427) and the aqueous phase (n = 1.334) do not match, there is an error in the calculation of the film thickness. The optical correction method proposed by Han and Shikazono [13] and Mac Giolla Eain et al. [50] was employed to calculate the actual film thickness. By considering the wall curvature and the refractive index difference, it was found that the error in the film thickness is between 8.36–14.48% for all conditions studied. The effect of gravity can be neglected in the present work as the Bond number, Bo, (ratio of gravitational over surface tension forces) is significantly less than 1 (0.016 and 0.052 in the 0.2 mm and the 0.5 mm ID channels, respectively).

In small channels, the liquid film thickness is dominated by the balance between viscous and surface tension forces, represented by the Capillary number, Ca [13,17]. The normalized ionic liquid film thickness δ/D against the Capillary number is shown in Fig. 5 for equal phase flow rates $Q_{aq} = Q_{IL} = 0.653$–35.34 ml/hr. The Ca number was calculated based on the plug velocity ($Ca = \mu_{IL}U_p/\sigma$) and varied between 0.0224 and 0.299. The Ca values are about 9.82–25.14% larger than those based on mixture velocity (U_{mix}).

As can be seen in Fig. 5, the dimensionless film thickness increases non-linearly with increasing Capillary number. The dimensionless film thickness is slightly lower in the 0.2 mm ID channel compared to the 0.5 mm ID one for the same Ca. Also shown in the figure are plots of literature correlations as given in Table 1. The Bretherton [51] model fails to predict the film thickness for both channels tested, as the current Ca numbers exceed the prediction range of this model ($Ca < 0.003$). The fitting parameters in the correlations proposed by Irandoust and Andersson [52] and Aussillous and Quéré [53], which are based on gas-liquid flows, have been modified from least square regression analysis of the current experimental data. These models show that the film thickness is solely related to the Capillary number, and ignore the effects of inertial forces at relatively high velocities. They therefore, predict better the experimental data at low Ca. Poor agreement was found between the experimental data and the Dore et al. [36] model, which was developed for liquid-liquid plug flow, with a deviation between 6.63–73.76% (40.19% on average).

Han and Shikazono [13] proposed a correlation for gas-liquid flows which accounts for the effects of surface, viscous and inertial

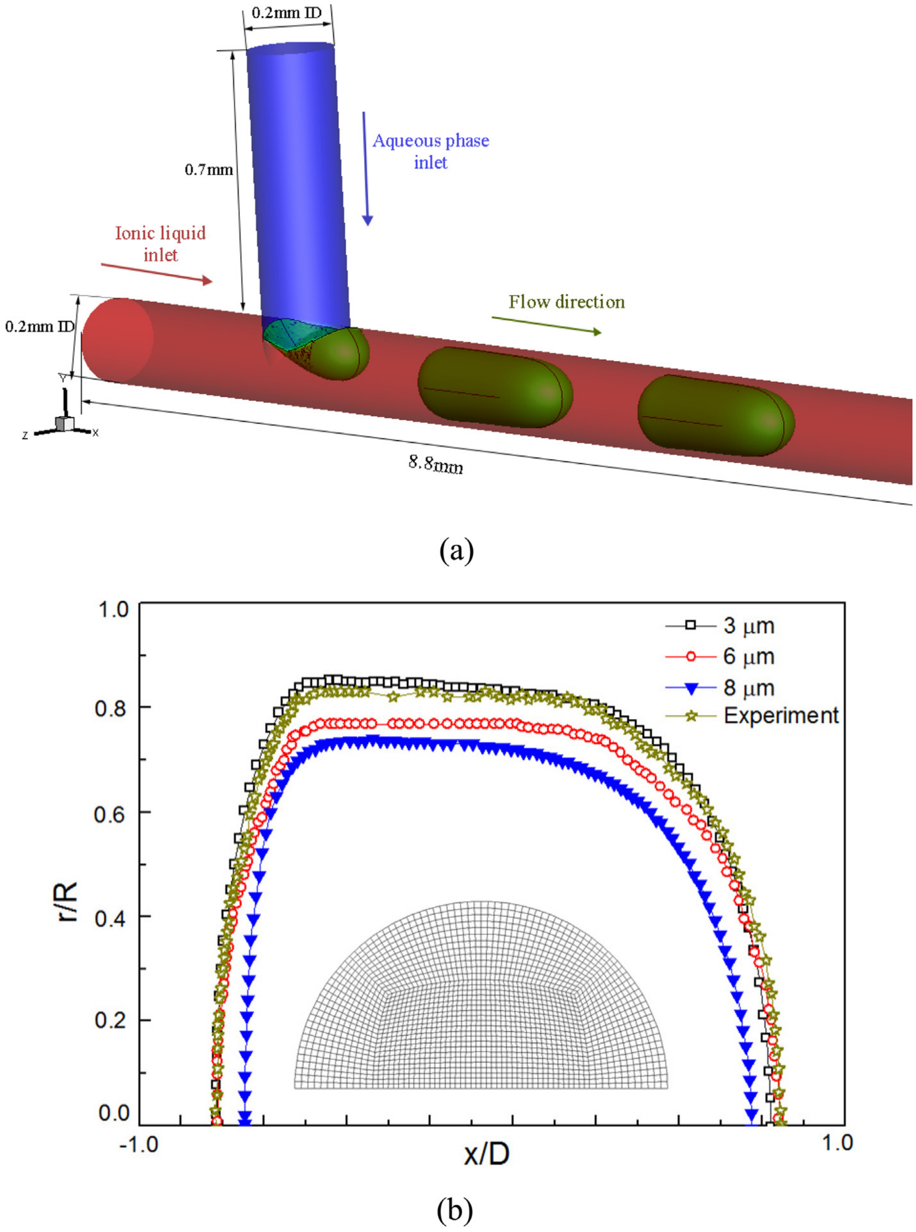

Fig. 4. (a) Schematic of the T-shaped computational domain in the 0.2 mm channel. The inlet channel lengths for the ionic liquid (continuous) and the aqueous (dispersed) phases are both 0.7 mm. The total length of the test section is 8.8 mm. (b) Grid dependence of plug shape at $Q_{aq} = Q_{IL} = 3.39$ ml/h in the 0.2 mm ID channel. Also shown is the computational mesh in half of the cross sectional plane.

forces by incorporating the Reynolds and Weber numbers in addition to Ca. Their model, however, overpredicts the film thickness by 11.24–88.19% (55.13% on average). The viscosity difference between the phases is considered to be responsible for the poor agreement. In gas – liquid flows, the shear forces between the phases can be ignored as the gas viscosity is negligible. In liquid-liquid flows, however, the reduced viscosity difference can increase significantly the interfacial shear forces. As a result, there may be non-negligible flow in the continuous film surrounding the plugs and the film thickness and plug velocity will be different to those in gas-liquid flows [50]. Langewisch and Buongiorno [54] suggested a film thickness correlation based on extensive numerical studies of gas-liquid slug flows (Table 1), which agrees well with the Han and Shikazono [13] model (deviation < 3.9%), but is over a broader range of Ca and Re numbers ($0.005 < Ca < 2$; $0 < Re < 900$). Mac Giolla Eain et al. [50] suggested a correlation from experimental data on liquid-liquid flows for $0.002 < Ca < 0.119$, where the We number was included to account for inertial forces at high velocities. The correlation agrees well with the current experimental data with a deviation of 0.64–16.8% (8.72% on average). An expression including Ca and Re numbers was suggested by Tsaoulidis and Angeli [22], for $0.03 < Ca < 0.18$, which however overpredicts the current experimental data by 1.57–34.61% (19.54% on average). The effect of channel size could be almost negligible in gas-liquid flows; using the Han and Shikazono [13] model an average difference in film thickness of only 0.722% at $0.0224 < Ca < 0.299$ was found between the 0.2 and 0.5 mm ID channels. In the current data, however, the average difference was 13.66% under the same conditions. An improved correlation, based on the Mac Giolla Eain et al. [50] model, is suggested

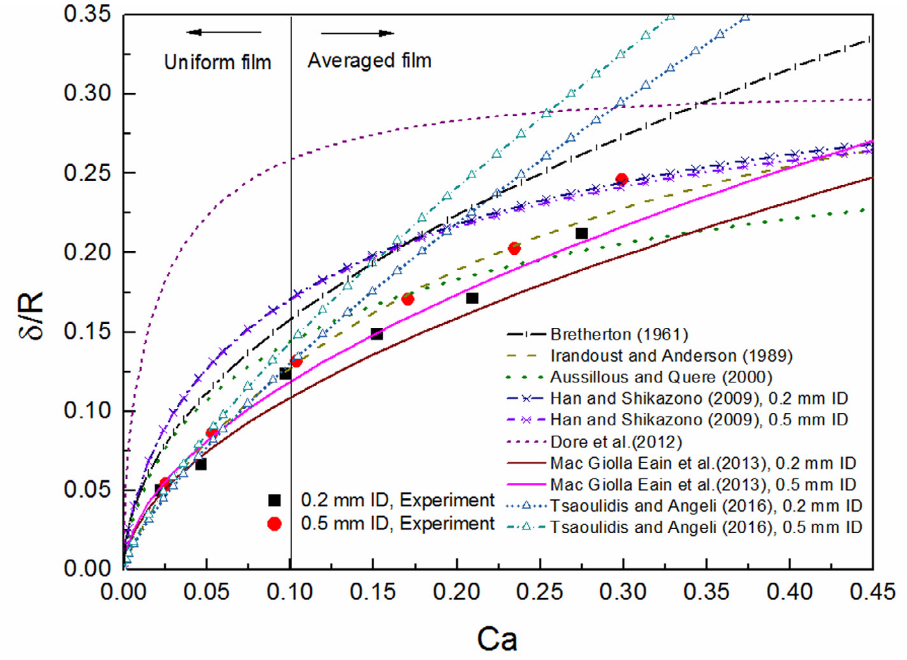

Fig. 5. Experimental non-dimensional film thickness against Capillary number in the 0.2 mm and 0.5 mm ID channels and comparison with literature correlations.

Table 1
Correlations of normalized film thickness (δ/R) for two-phase Taylor or plug flow.

Correlation	Parameters	Measuring technique	Reference
$\frac{\delta}{R} = 0.5Ca^{1/2}$	Ca < 0.003, gas – liquid Taylor flow	Conductimetry	Bretherton [51]
$\frac{\delta}{R} = 0.33[1 - \exp(-3.08Ca^{0.79})]$	$9.5 \times 10^{-4} < Ca < 1.9$, gas – liquid Taylor flow	Light absorption	Irandoust and Andersson [52]
$\frac{\delta}{R} = \frac{1.15Ca^{\frac{2}{3}}}{1+1.34(2.5Ca^{\frac{2}{3}})}$	$10^{-3} < Ca < 1.4$, gas – liquid Taylor flow	Video recording	Aussillous and Quéré [53]
$\frac{\delta}{R} = \frac{1.34Ca^{\frac{2}{3}}}{1+3.13Ca^{\frac{2}{3}}+0.504Ca^{0.672}Re^{0.589}-0.352w_e^{0.629}}$	Re < 2000, 0.002 < Ca < 0.16 gas – liquid Taylor flow	Laser focus displacement	Han and Shikazono [13]
$\frac{\delta}{R} = 0.3(1 - e^{-6.9Ca^{0.54}})$	0.007 < Ca < 0.159, liquid-liquid Taylor flow	Micro-PIV	Dore et al. [36]
$\frac{\delta}{R} = 0.35Ca^{0.354}We^{0.097}$	0.002 < Ca < 0.119, liquid-liquid Taylor flow	High speed image capture	Mac Giolla Eain et al. [50]
$\frac{\delta}{R} = \frac{1.34Ca^{\frac{2}{3}}}{1+[1+\varnothing(Re)]2.93\times Ca^{0.764}}$ $\varnothing(Re) = \left[\frac{33.1}{Re^{0.539}} + 0.000472Re^{1.909}\right]^{-1}$	0.005 < Ca < 2, 0 < Re < 900, gas-liquid Taylor flow	Open source CFD code (Gerris)	Langewisch and Buongiorno [54]
$\frac{\delta}{R} = 0.658Ca^{0.6409}Re^{0.1067}$	0.03 < Ca < 0.18, liquid-liquid Taylor flow	High speed image capture	Tsaoulidis and Angeli [22]

(Eq. (2)) that is valid for Ca between 0.0224 and 0.299, with deviation 0.27%–11.26% (6.77% on average) from the experimental data.

$$\frac{\delta}{R} = 0.385Ca^{0.265}We^{0.098} \tag{2}$$

3.2. Plug velocity

The plug velocity is shown in Fig. 6 for both the 0.2 mm and 0.5 mm ID channels for equal phase flow rates $Q_{aq}=Q_{IL}=0.653$–35.34 ml/hr. The plug velocity is always higher than the mixture velocity, because of the film which surrounds the plugs. With increasing mixture velocity, the normalized film thickness (δ/R) in both channels increases, leading to a larger deviation between U_{mix} and U_p. It can also be seen that the plug velocity in the 0.5mm ID channel is higher than in the 0.2mm channel by 5.42–14.48% for the same mixture velocity ($0.005 < U_{mix} < 0.03$ m/s), which is expected since the film thickness is also larger in the 0.5 mm channel. The experimental results are compared with literature correlations from gas-liquid and liquid-liquid systems, as summarized in Table 2. Since the plug velocity is related to the film thickness, the correlations in their majority include the Capillary number or the film thickness.

The correlation by Bretherton [51] overpredicted the experimental results with average deviation of 36.91%; as was mentioned above the model was developed for Ca < 0.003. The model by Liu et al. [55] showed good agreement with the experimental data, with average deviations of 6.91% and 12.76% for the 0.2 and 0.5 mm channels respectively. However, their correlation only includes the effect of Capillary number but not the channel size. The correlation by Kashid et al. [7] developed from experimental data on liquid-liquid plug flow, includes the film thickness rather than the Ca and agrees very well with the current data with an average deviation of 5.85%. A similar expression was proposed by Langewisch and Buongiorno [54] for gas-liquid Taylor flow, which

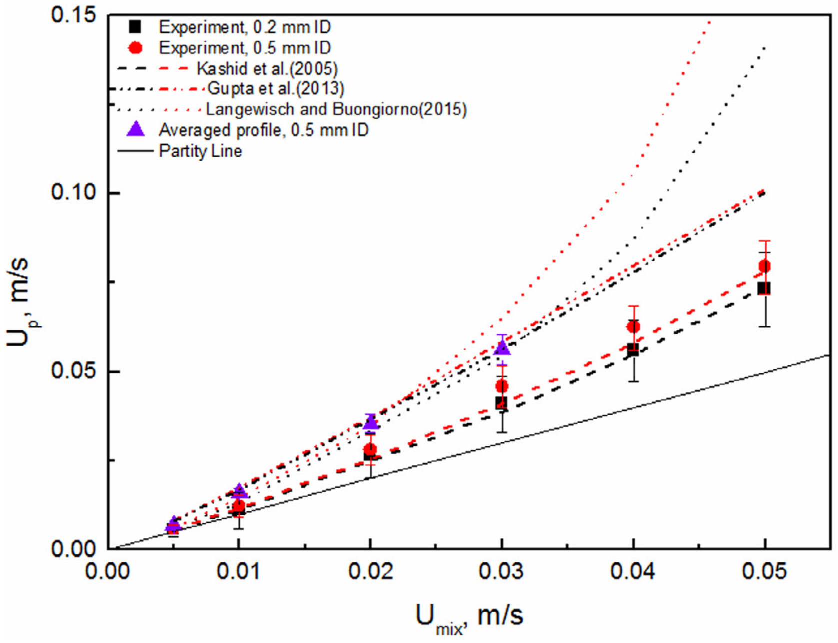

Fig. 6. Experimental plug velocity against mixture velocity in the 0.2 mm and 0.5 mm ID channels and comparison with literature correlations.

Table 2
Correlations of plug velocity for two-phase Taylor and plug flows.

Correlation	Parameters	Reference
$\frac{U_p-U_s}{U_p}=1.29(Ca)^{2/3}$	Ca < 0.003, gas – liquid Taylor flow	Bretherton [51]
$\frac{U_p}{U_{mix}}=\frac{1}{1-0.61Ca^{0.33}}$	$2\times10^{-4}<Ca<0.39$gas – liquid Taylor flow	Liu et al. [55]
$\frac{U_p}{U_{mix}}=\frac{2}{1+(R_p/R)^2}$	0 < U_{mix}<0.2 m/s, liquid - liquid Taylor flow	Kashid et al. [7]
$\frac{U_p}{U_{mix}}=\frac{\left[2+\left(\frac{R_p}{R}\right)^2\right]\left(\frac{1}{\lambda}-2\right)}{\left[1+\left(\frac{R_p}{R}\right)^4\right]\left(\frac{1}{\lambda}-1\right)}$	0.076 < U_{mix}<0.151 m/s, 0.0045 < Ca < 0.0089 liquid - liquid Taylor flow	Gupta et al. [12]
$\frac{U_p}{U_{mix}}=\left(1-2\frac{\delta}{D}\right)^{-2}$	0.005 < Ca < 2, 0 < Re < 900 gas – liquid Taylor flow	Langewisch and Buongiorno [54]

however overpredicts the experimental data by 9.94–68.21%. This difference is expected since the model did not predict well the film thickness compared to the current results. Gupta et al. [12] proposed a correlation for liquid-liquid flow by combining the effects of viscosity ratio and film thickness, which however overpredicts the current results by 3.55–29.16%.

The velocity profiles inside the aqueous phase plugs were obtained with μPIV as discussed in Section 2. An example of average profiles, obtained from 30 instantaneous velocity fields, is shown in Fig. 7 (a) for $Q_{aq} = Q_{IL} = 7.068$ ml/h ($L_p = 1.155$ mm) in the 0.5mm ID channel. Since the refractive index of the two phases is not matched there are reflections close to the interface particularly at the plug front and rear where the interface curvature is high and velocity fields cannot be obtained in these areas.

The profiles of the horizontal velocity component, non-dimensionalised with the maximum velocity, are shown in Fig. 7 (b) for 13 axial locations along the plug. The spacing between the profiles is 104.25 μm. All profiles have a parabolic shape with the peak located near the centreline of the channel (r/R = 0.091). The maximum velocity is found at the plug centre (X/Lp = 0.522). Moving towards the liquid/liquid interfaces at the plug front and back, the velocity reduces and the profiles become more flat. The average plug velocities can also be calculated by spatially averaging these time-ensemble profiles [35,56] and is shown in Fig. 6. As can be seen, they are higher than those calculated from plug displacement by 4.47–10.99%, which is expected because the profiles close to the front and rear of the plug, where velocities are low, could not be measured. The plug velocity based on the tip displacement method will be used subsequently.

3.3. Plug length

The dimensionless plug lengths in both channels were found to be $1.14 < L_p/D < 2.48$ and fall into the transition regime ($1 < L_p/D < 2.5$ for circular T-junction microchannels) where the shear stresses, the surface tension and the pressure difference are all affecting the forming plug [20,21,57,58]. In this regime, both the Capillary number and the phase flow rate ratio should be considered. The dimensionless plug length is plotted against Ca (based on plug velocity; Fig. 8a) and Q_{aq}/Q_{IL} (Fig. 8b) for the 0.2mm and 0.5mm ID channels, as well as against the mixture velocity for equal flowrates in the inset graph in Fig. 8a. The effect of wall curvature and refractive index difference on plug length is less than 5% for all conditions studied, using the method discussed in Section 3.1. As can be seen, L_p/D decreases with increasing U_{mix} at equal phase flow rates, while it is larger in the 0.2mm channel compared to the 0.5 mm ID one by 6.40–23.68% under the same U_{mix}. The dimensionless length in both channels can be scaled with Ca as $L_p/D \sim Ca^{-0.273}$, and with the flowrate ratio as $L_p/D \sim (Q_{aq}/Q_{IL})^{0.512}$. Since both Ca and flow rate ratio affect the plug length in the transition regime a correlation is proposed (Eq. (3)) based on that developed by Xu et al. [20], which agrees well with the experimental data, with an average deviation of 13.13%:

$$\frac{L_p}{D} = 0.757(Q_{aq}/Q_{IL})^{0.512}Ca^{-0.273} \tag{3}$$

The plug lengths predicted from Eq. (3) agree slightly better with the experimental data for the 0.5 mm channel (deviation of 6.03%) compared to the 0.2 mm one (deviation of 8.81%). In the small channel, the plug lengths are more sensitive to pressure variations from the formation of the plugs or their exiting from the channel which could explain the increased deviation. A number

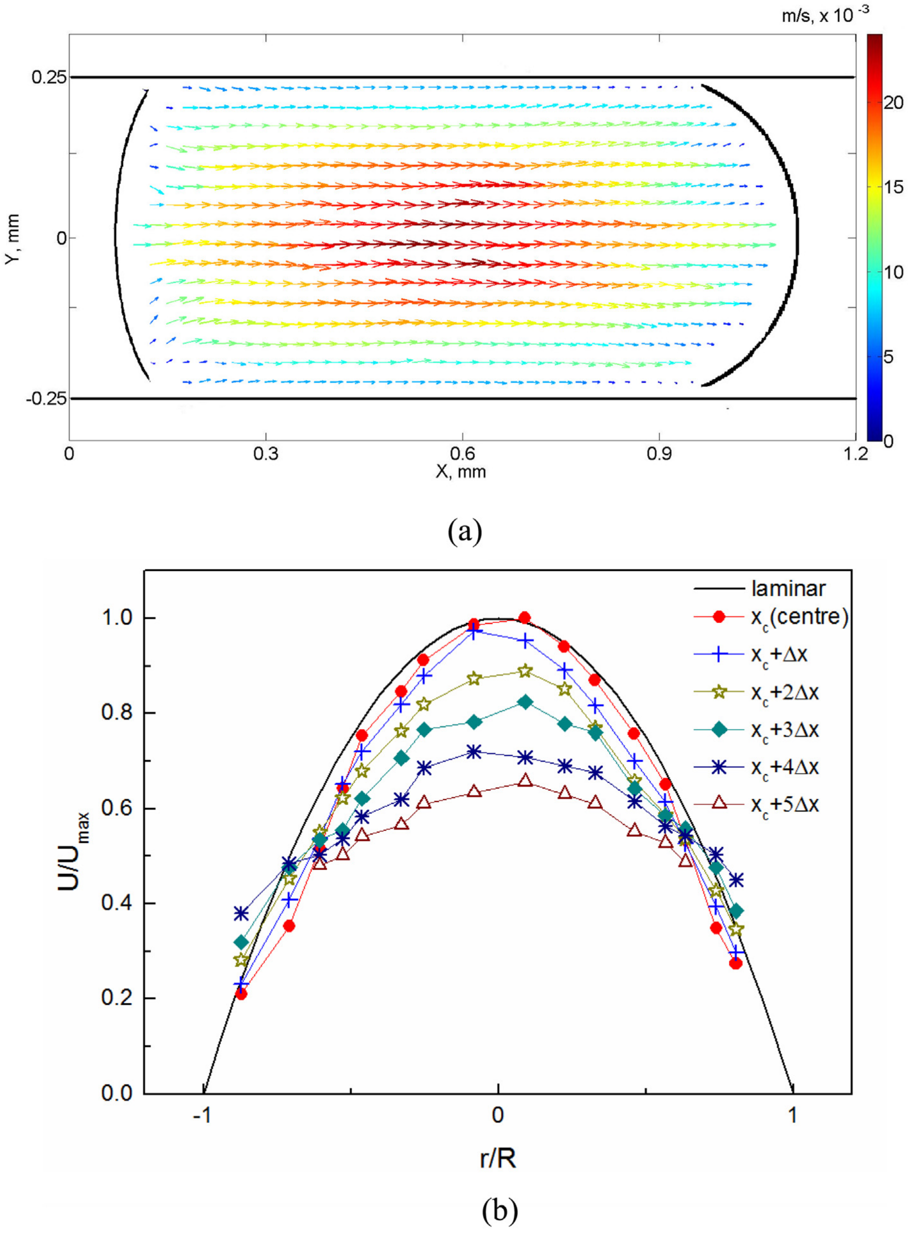

(a)

(b)

Fig. 7. (a) Ensemble average velocity field inside the plug at $Q_{aq} = Q_{IL} = 7.068$ ml/h in the 0.5 mm ID channel. The magnitude of the velocity is shown in colour (Lp = 1.155 mm); (b) Non-dimensional horizontal component of total velocity at different locations along a plug, for $Q_{aq} = Q_{IL}$=7.068 ml/h in the 0.5 mm ID channel. The spacing between each profile is approximately 104.25 μm.

of different correlations have been developed in the literature to estimate the plug length in two-phase flows, either empirically or from physical models of the plug formation mechanism. Representative correlations are summarized in Table 3 and the empirical ones are compared with the experimental results in Fig. 9. Laborie et al. [59] developed an empirical correlation from gas-liquid flow studies in 1–4 mm ID vertical circular channels at relatively high velocities (0.1–1 m/s). The gas bubble length was found to increase with increasing superficial velocities, contrary to the current observations. Qian and Lawal [60] from numerical simulations of gas-liquid flow in a T-junction microchannel, proposed a correlation for different inlet geometries, superficial velocities and fluid properties, and found that the dimensionless length depended mainly on Re, Ca and gas hold up, ε_G. Similar models were also proposed by Sobieszuk et al. [61] and Tsaoulidis and Angeli [22], which however over predict the results by 94.04–157.16% and 22.45–81.26% respectively. The correlations by Garstecki et al. [18] and Prileszky et al. [62], developed from considerations of the plug formation mechanism, are applicable to very low Ca. Fu et al. [58] proposed a plug length correlation for liquid-liquid flow in rectangular channels, which predicts the current data with a mean relative deviation of 32.29%.

3.4. Plug volume and shape

One of the main advantages of microfluidic systems is the ability to control the size and volume of the dispersed phase. The volume of individual plugs was calculated by 3D rotation of the detected interface along the channel centerline and is shown in Fig. 10 for equal flow rates of the two phases in both the 0.2mm and 0.5mm ID channels. At high mixture velocities, the relative long camera exposure time used slightly blurs the plug

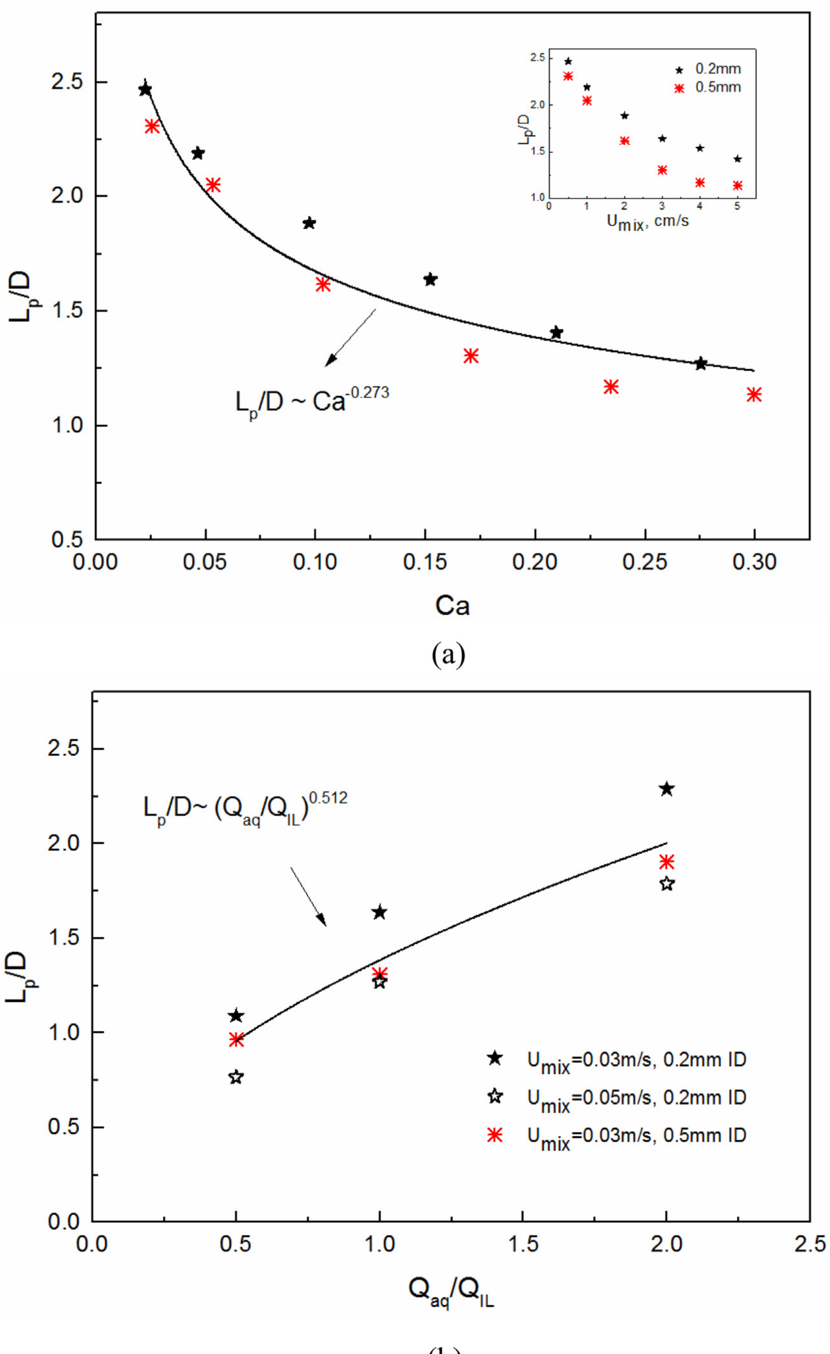

(a)

(b)

Fig. 8. Dimensionless plug length L_p/D against (a) Capillary number, Ca, for equal phase flow rates, and (b) flow rate ratio, Q_{aq}/Q_{IL}, in the 0.2 mm and 0.5 mm ID channels. Inset in (a) shows the dependence of L_p/D on U_{mix} for equal phase flow rates.

interface. This increases the uncertainty of locating the interface and the error when estimating the plug volume (about 10.49%). As can be seen from Fig. 10 the channel size has a profound effect on plug volume where an increase in the channel diameter from 0.2 mm to 0.5 mm increases the volume by 13–17 times. With increasing mixture velocity, the plug volume decreases in both channels because the plug length and width (due to thicker ionic liquid film around the plug) decrease. The non-dimensional equivalent diameter d*, defined as the ratio of diameter of a spherical droplet with the same volume as the plug to the channel diameter, decreases with increasing U_{mix}, but is barely affected by the channel size.

At very low Capillary numbers ($0.004 < Ca < 0.009$), the plugs reach volume-independent shapes for $d^* > 1.1$ [12,63], where only the droplet length changes with mixture velocity but the leading and trailing plug menisci are unaffected. However, at the high Capillary numbers of the current study ($0.0224 < Ca < 0.299$), both the front and the tail plug menisci change shape with velocity. The radii of the front and tail plug ends are presented in Fig. 11. At the lowest Ca (U_{mix}=0.005 m/s), both plug ends resemble a hemisphere with dimensionless radius close to unity; the $r^*_{tail} = r_{tail}/R \approx 1$, while the front meniscus radius is smaller, $r^*_{front} = r_{front}/R = 0.76$. As the Capillary number increases the radius of the front plug cap decreases (curvature increases) while the rear cap

Table 3
Correlations of normalized plug length (L_p/D) for two-phase Taylor and plug flows.

Correlation	Taylor flow type	Parameter	Reference
$\frac{L_p}{D} = 0.0878\frac{Re_p^{0.63}}{Eo^{1.26}}$ $Re_V = \frac{\rho U_p D}{\mu}\ E_o = \frac{\rho D^2 g}{\sigma}$	gas – liquid flow in 1–4 mm circular channel	$1.5\ x10^{-3} < Ca < 0.1$	Laborie et al. [59]
$\frac{L_p}{D} = 1.637\varepsilon^{0.107}(1-\varepsilon)^{-1.05}Re^{-0.075}Ca^{-0.0687}$	gas – liquid flow T-junction, 2D simulation	$0.09 < \varepsilon < 0.91$ $15 < Re < 1500$ $2.78\ x\ 10^{-4} < Ca < 0.01$	Qian and Lawal [60]
$\frac{L_p}{D} = 1 + \alpha\frac{Q_d}{Q_c}$	Liquid/gas–liquid flow, rectangular channel, T-junction	$Ca < 10^{-2}$	Garstecki et al. (2006)
$\frac{L_p}{D} - \varepsilon = k(Q_d/Q_c)^{\alpha}Ca^{\beta}$	Liquid-liquid flow Rectangular channel, T-junction	$10^{-4} < Ca < 0.3$	Xu et al. [20]
$\frac{L_p}{D} = 1.3\varepsilon^{0.07}(1-\varepsilon)^{-1.01}We^{-0.1}$	gas – liquid flow square/circular/rectangular channel, Y-junction	$0.1 < We < 26$ $0.02 < U_p < 1.2$ m/s $0.06 < \varepsilon < 0.85$	Sobieszuk et al. [61]
$\frac{L_p}{D} = 0.72(Q_d/Q_c)^{0.14}Ca^{-0.19}\ (L_p/D < 2.35)$ $\frac{L_p}{D} = 0.30(Q_d/Q_c)^{0.23}Ca^{-0.42}\ (L_p/D > 2.35)$	Liquid-liquid flow Rectangular channel, co-flow	$0.001 < Ca < 0.01$	Fu et al. [58]
$\frac{L_p}{D} = 2.282 \cdot Ca^{0.2728} \cdot Re^{0.4617} \cdot Re_c^{-0.9634}$	Liquid-liquid flow Rectangular channel, T-junction	$0.03 < Ca < 0.18$	Tsaoulidis and Angeli [22]
$\frac{L_p}{D} = \theta_0 + \theta_1\frac{Q_d}{\mu Q_c}$	Liquid-liquid flow Circular channel, T-junction	$0.001 < Ca < 0.01$	Prileszky et al. [62]

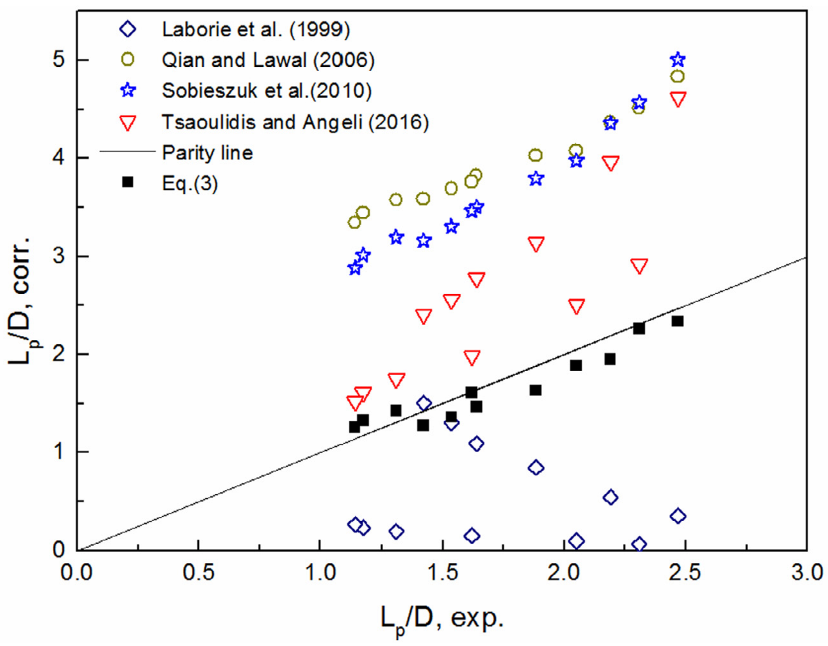

Fig. 9. Comparison of the experimental dimensionless plug lengths with the correlations listed in Table 3 in the 0.2 mm and 0.5 mm ID channels.

becomes more flat and its curvature decreases. The channel size does not affect the plug shape significantly and there is only a difference of 1.87–6.11% between the two channels. It affects, however, more the front cap shape with a difference of 10.57–37.38% between the two channels for the same mixture velocities. Therefore the variations in the thickness of the liquid film surrounding the plug are mainly affected by changes in the front plug cap.

3.5. Velocity profiles

The velocity profiles in the aqueous plug phase obtained from the CFD simulations and the PIV measurements are shown in Fig. 12(a) and are compared with the laminar profile for $U_{mix} = 0.01$ m/s in the 0.5 mm ID channel ($Q_{aq} = Q_{IL} = 7.068$ ml/hr, Lp/D = 2.28). The profiles have been non-dimensionalised using the averaged maximum velocity (at the centre of the plug). In the numerical simulations, the U_{max} inside the aqueous plug was obtained by comparing the velocities in the dispersed phase using a user defined function. The measurements were taken at 2.05R from the plug front, which is almost free from the rear and front effects. The results are also compared against the profiles given by Eqs. ((4)–(6)) for ideal annular flow with a known film thickness at a certain mixture velocity [12,23,63]:

Plug region: $0 < r < R_p$

$$U_{x,p} = 2U_{mix}\frac{\left[\left(1-\frac{R_p^2}{R^2}\right)+\frac{1}{\lambda}\left(\frac{R_p^2}{R^2}-\frac{r^2}{R^2}\right)\right]}{\left(1+\frac{R_p^4}{R^4}\right)\left(\frac{1}{\lambda}-1\right)} \tag{4}$$

Film region: $R_p < r < R$

$$U_f = 2U_{mix}\frac{\left(1-\frac{R_p^2}{R^2}\right)}{\left(1+\frac{R_p^4}{R^4}\right)\left(\frac{1}{\lambda}-1\right)} \tag{5}$$

$$U_{x,f} = 2U_f\frac{1-\frac{r^2}{R^2}}{1-\frac{R_p^2}{R^2}} \tag{6}$$

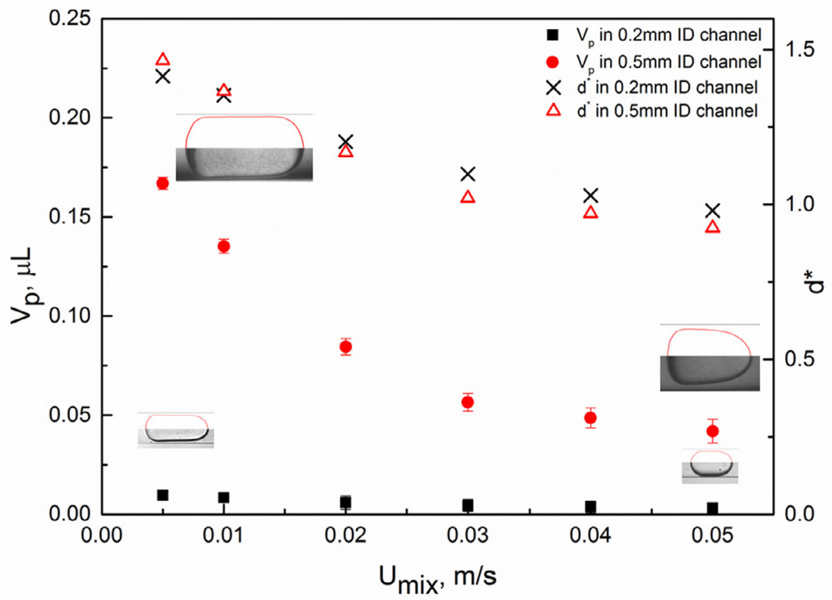

Fig. 10. Plug volume and non-dimensional equivalent plug diameter against mixture velocity for $Q_{aq} = Q_{IL} = 0.653–35.34$ ml/hr in the 0.2 mm and 0.5 mm ID channels.

where $U_{x,p}$ and $U_{x,f}$ are the velocity distributions in the aqueous plug and the ionic liquid film respectively, U_f is the average film velocity, λ is the ratio of the plug to the continuous phase viscosity, and $R_p = R - \delta$ is the plug radius in the middle of the plug. To develop the above model it was assumed that a uniform film thickness exists around the plug and the flow in the plug region is annular with equal pressure drop in both phases. A similar model for the film velocity profile was proposed by Fouilland et al. [64], from time resolved PIV measurements in gas-liquid flows:

$$U_{x,f} = U_{mix}\frac{1-\frac{R_p^2}{R^2}}{1+\frac{R_p^4}{R^4}\left(\frac{1}{\lambda}-1\right)} \qquad (7)$$

As can be seen from Fig. 12(a) there is good agreement between the CFD simulations and the experimental average velocity profiles in the plug (average deviation 20.94%), particularly in the centre of the channel. Close to the channel wall there is larger uncertainty in the PIV velocity measurements (up to 26.94%) due to high interface curvature. The differences of Eq. (4) from the laminar profile ($U = U_{max}(1 - r^2/R^2)$) indicate that the plugs are not long enough for the velocity to become fully developed even in the middle of the plug. The velocity profile in the film is shown in Fig. 12(b), where the CFD predictions are compared against Eqs. (6) and (7). Near the wall the CFD simulations have spatial resolution of 2–3 μm in the 0.5mm ID channel. The results indicate a Couette local velocity profile. The maximum velocity occurs at the plug surface, while the maximum film velocity ($U_{f,\ max}$) is much smaller than the U_{max} within the plug. The profile predicted by Eq. (7) [64] agrees better with the CFD results with a difference up to 19.78%. The CFD model slightly underpredicts the experimental film thickness by 3.37%.

The velocity profiles in both the plug and the film at the middle of the plug for two different mixture velocities, 0.01 m/s and 0.03 m/s in the 0.2mm ID channel under equal phase flow rates are shown in Fig. 13. The velocities obtained from the CFD simulations are about 5.85% different from the ones found from Eq. (4) for U_{mix}=0.01 m/s. The difference increases to 16.92% for U_{mix}=0.03 m/s because in this case the plug length and width decrease and the film surrounding the plug becomes non-uniform. This also causes larger deviation from the laminar profile as U_{mix} increases. Overall, using the velocity profile correlations by Gupta et al. [12], Eq. (4), for the central region of the plug and by Fouilland et al. [64], Eq. (7), for the film, the flow field can be satisfactorily described for axial locations in the middle of the plugs.

The circulation patterns in the plugs can be found by subtracting the plug velocity from the average velocity profiles. The patterns from both the PIV measurements and the CFD simulations are shown in Fig. 14a, for U_{mix} = 0.01 m/s in the 0.5 mm channel ($Q_{aq} = Q_{IL}$ = 7.068 ml/hr). The results are in good agreement and show two main vortices on the upper and the lower parts of the channel. The vortex centers are located in both cases at around $r^0/R = 0.747$ (r^0 is the distance of the stagnation point from the channel centre), which agrees with the value of 0.718 given by Thulasidas et al. [65]. Two smaller counter-clockwise vortices in Fig. 14b, at the front and rear cap of the plug, are predicted by the simulations but cannot be detected in the PIV measurements as the velocity field is not well resolved in these areas. These vortices are attributed to the changes in Laplace as well as tangential stresses as the plug shape changes from the front or the end tips to the middle part of the plug. The Laplace pressure at the front or the back of the plug is $\Delta P = \gamma\ (1/R_1+1/R_2)$, where R_1 and R_2 are the two principal radii of curvature of the interface, while in the main body of the plug which has cylindrical shape it is $\Delta P = \gamma/R_1$ (R_2 approaches infinity; [32]). In addition, the shear stresses near the interface change as the film thickness varies from the plug ends to the middle [66]. For low viscosity plugs ($\lambda<<1$, $\lambda = \mu_{aq}/\mu_{IL}$), the ionic liquid in regions A and B (Fig. 14b) drives the recirculating flow inside the plugs after deformation [67]. The very small vortices at the front of the primary ones near the channel axis, are considered to be spurious results generated numerically [68].

The circulation patterns are influenced not only by the flow velocity, but also the channel size as can be seen by comparing Fig. 14b with Fig. 15a for U_{mix}=0.01 m/s in the 0.5 mm and the 0.2 mm channels respectively. In the small channel the stagnation point of the main circulation is closer to the channel wall compared to the 0.5 mm channel, at around $r^0/R = 0.764$ (4.58% different from the value of $r^0/R = 0.729$ given by Thulasidas et al. [65]). The small vortices at the two plug ends in the 0.2 mm channel

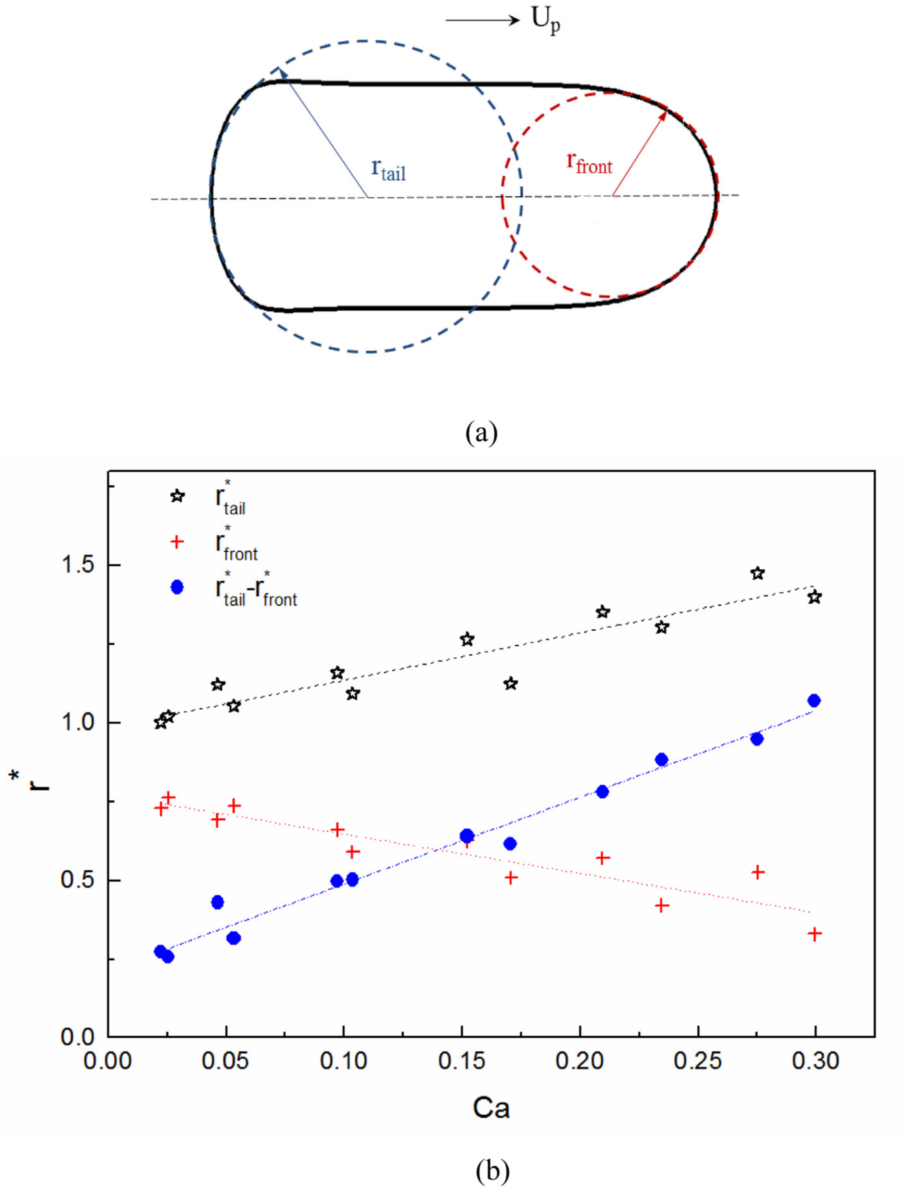

Fig. 11. (a) Schematic of a plug at $Q_{aq} = Q_{IL} = 7.068$ ml/h in the 0.5 mm ID channel; (b) Dimensionless radius of the leading and trailing plug menisci against Capillary number for $Q_{aq} = Q_{IL}$=0.653 – 35.34 ml/hr in the 0.2 mm and 0.5 mm ID channels.

are slightly weeker, due to the more curved hemispherical caps. The effect of mixture velocity can be seen by comparing Fig. 15a and b for U_{mix}=0.01 m/s and U_{mix}=0.03 m/s respectively in the 0.2 mm channel. With increasing U_{mix}, the cores of the main vortices move towards the centre of the plug, suppressing the secondary vortices at the two ends until they completely disappear. The simulation results agree well with those by Lac and Sherwood [63] and experimental findings by Meyer et al. [69].

A comparison of the velocity distribution at different channel cross sections along the plug is given in Fig. 16 for U_{mix}=0.03 m/s in the 0.2 mm channel. The total velocity magnitude is significantly larger in the plug centre (plane b) and the plug main body compared to the ends (planes a/c). In the main part of the plug, the velocity also has a strong axial component and the radial velocity is very small. At the two plug ends, the radial velocity component is increased. This increased radial velocity at the plug ends can significantly enhance mass transfer between the two phases via the interface and explains why 99% of mass transfer has been found to happen in the cap regions of the plug compared to the film region [10].

3.6. Pressure variation

The pressure in the channel was also calculated from the CFD simulations and an example of the profile along the 0.2mm ID channel is shown in Fig. 17 for Q_{aq}=Q_{IL}=3.39 ml/hr. The capillary contains a succession of dispersed plugs and slugs of the continuous fluid, separated by transition regions around the interfaces. The pressure gradient in the fully developed continuous slug can be described by the Hagen-Poiseuille law, while each plug has an additional component due to the Laplace pressure at the interfaces.

The detailed wall pressure distribution along a plug calculated from CFD is shown in Fig. 18 for three different cases. The tails of the plugs have all been brought to the same axial location, while the minimum pressure of all cases has been shifted to 0 to facilitate

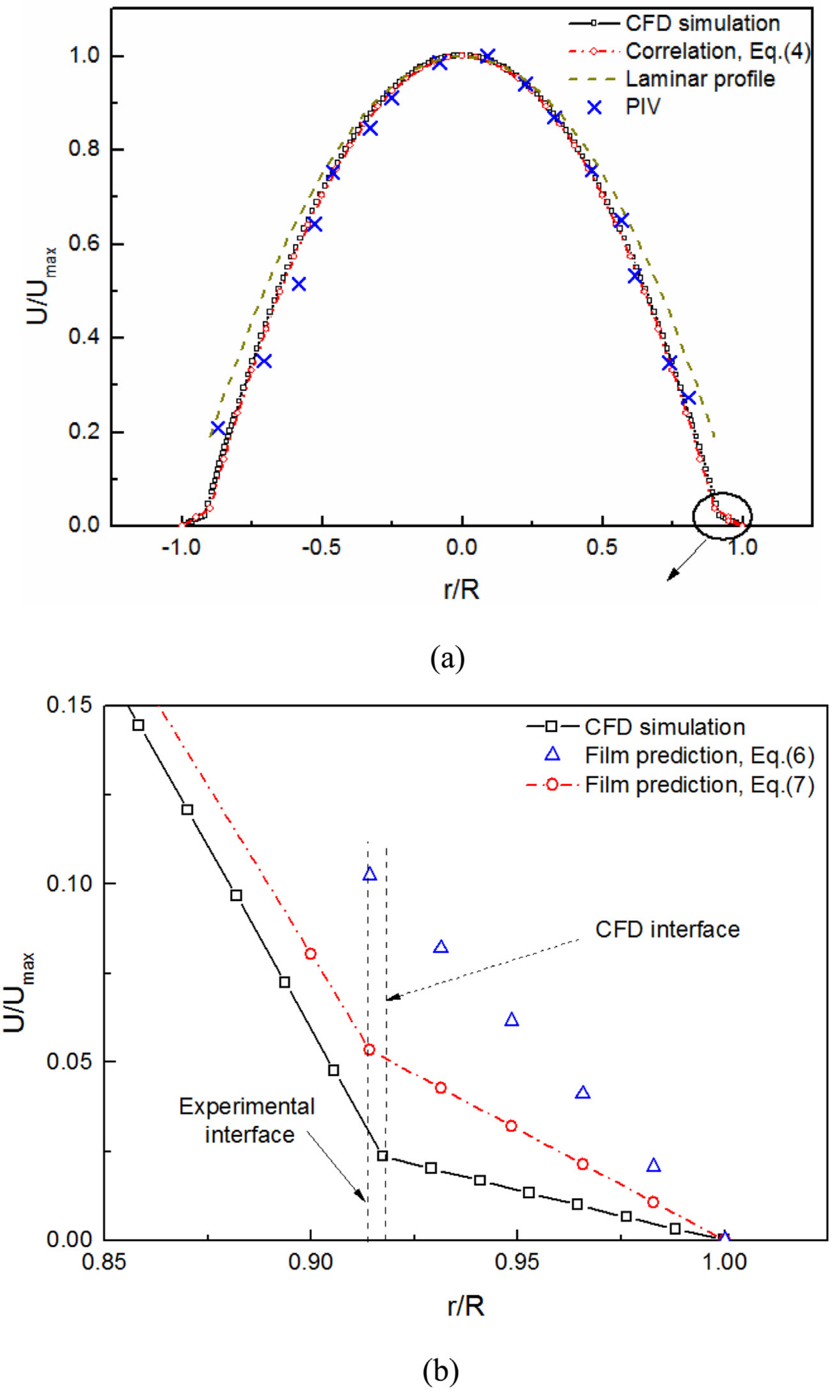

Fig. 12. (a) Comparison of the velocity profiles from the CFD simulations and the PIV measurements for $Q_{aq} = Q_{IL} = 7.068$ ml/hr in the 0.5 mm ID channel at a distance of 2.05 R from the plug front tip. Also shown are the laminar profile and the one predicted by Eq. (4). (b) Velocity profiles predicted from Eqs. (6) and (7) and the CFD simulations.

the comparisons. The dotted line represents the projected pressure based on a linear regression of the pressure variation before and after the plug in the continuous phase slug, which follows the Hagen-Poiseuille law. A typical wall pressure variation for a sufficiently long plug is given by U_{mix}=0.01 m/s in the 0.5 mm ID channel case. Within the continuous phase slug, the pressure decreases linearly because of friction. When the interface at the plug rear is reached, the pressure first decreases, probably because at this region the laminar flow profile is disturbed, and then increases sharply because of the Laplace pressure. In the film region the pressure decreases slightly (as the liquid in the film is nearly stagnant) until the front of the plug is reached, where it reduces significantly. In the slug phase the pressure continues to reduce due to friction. Compared to the profiles in the 0.2 mm ID channel, the Laplace pressure (increase in pressure at the plug rear) in the 0.5 mm channel is much smaller at the same U_{mix}. In the small channel, however, no uniform pressure decrease is observed in the plug as the film does not have a uniform thickness especially at U_{mix}=0.03 m/s where the plug is short.

The total pressure drop for a unit cell (plug + slug) can be calculated as the sum of the single phase pressure drop and an additional Laplace pressure component as follows [24,25]:

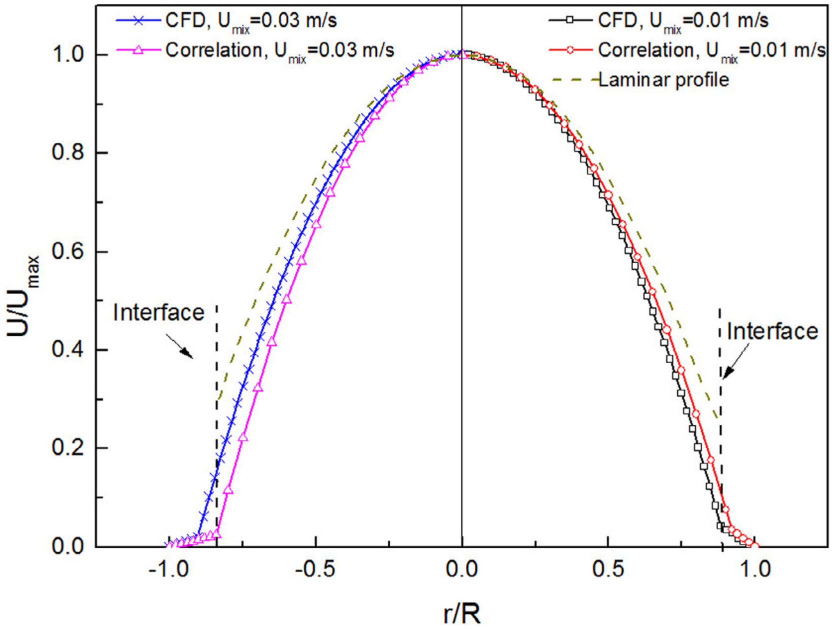

Fig. 13. Comparison of the velocity profiles in the centre of the plug obtained from the CFD simulations with those predicted by Eq. (7) for $Q_{aq} = Q_{IL}$ = 1.131 ml/hr (right) and $Q_{aq} = Q_{IL}$ = 3.393 ml/hr (left) in the 0.2 mm ID channel. The laminar flow profile is also shown.

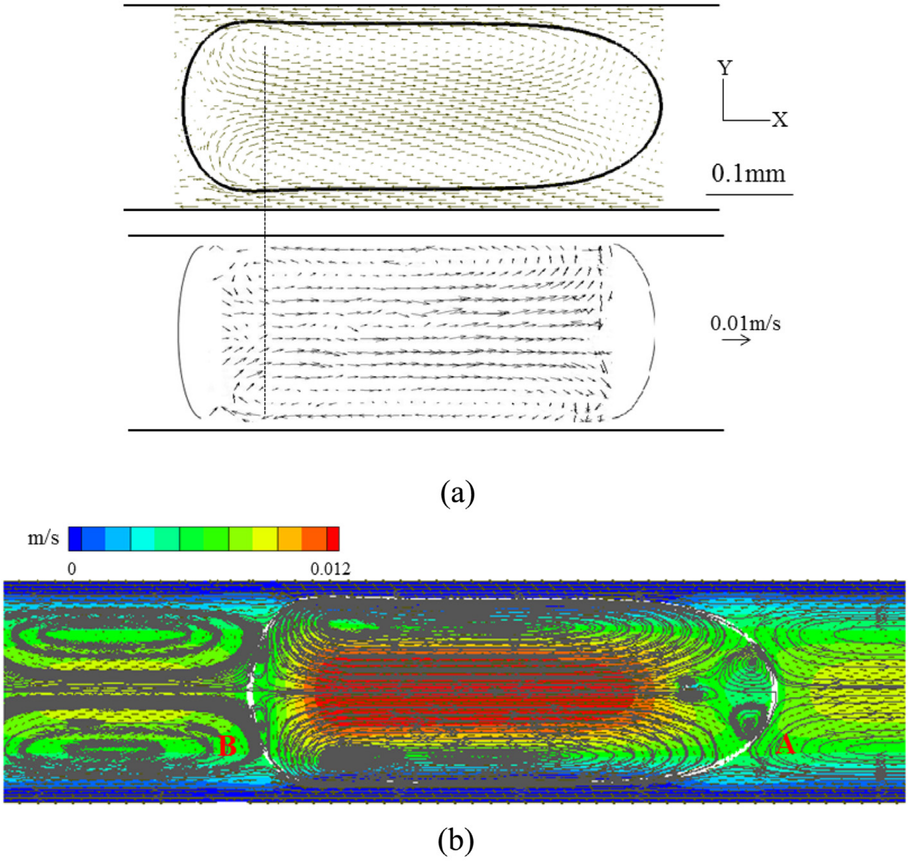

Fig. 14. (a) Comparison of velocity distribution and internal recirculation in a plug at U_{mix} = 0.01 m/s in the 0.5 mm ID channel for $Q_{aq} = Q_{IL}$ = 7.068 ml/hr from CFD simulations (top) and PIV measurements (bottom). (b) Numerical recirculation patterns in both phases for the same operation conditions. The velocity magnitude is superimposed in colour.

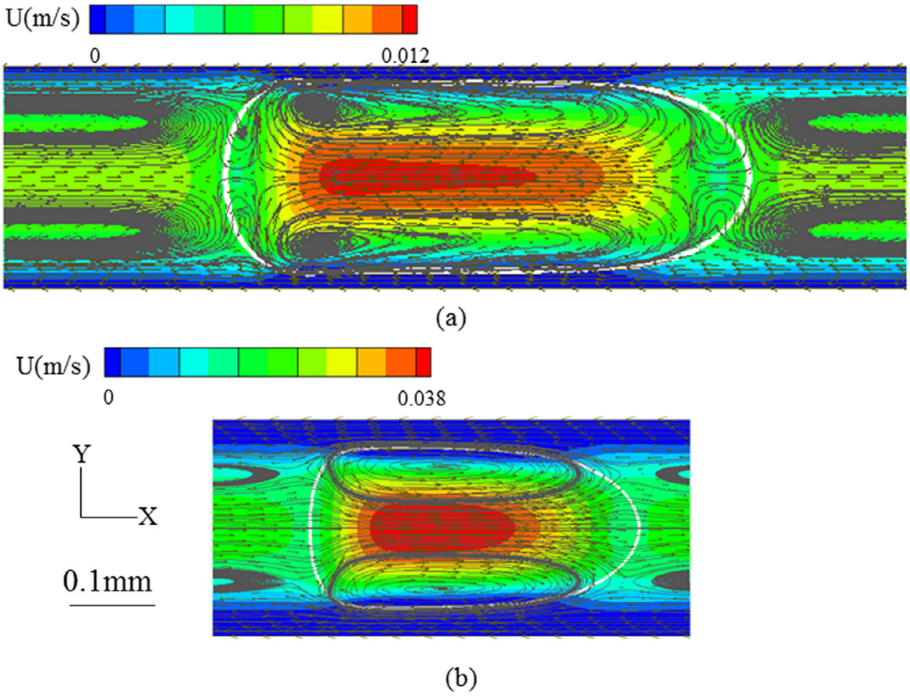

Fig. 15. Velocity distribution and internal recirculation in a plug from CFD simulations at (a) $U_{mix} = 0.01$ m/s and (b) $U_{mix} = 0.03$ m/s, in the 0.2 mm ID channel for $Q_{aq} = Q_{IL} = 1.131$ ml/hr (a) and 3.393 ml/hr (b) ml/hr. The velocity magnitude is superimposed in colour.

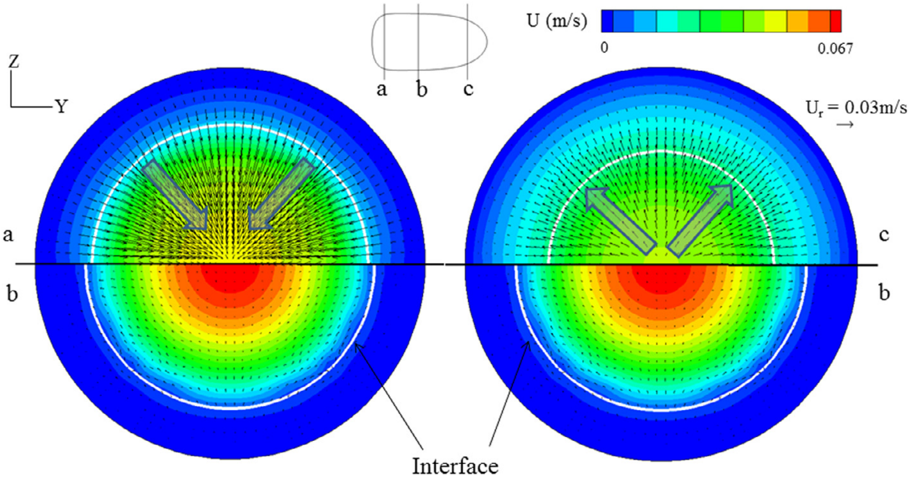

Fig. 16. Velocity distribution in different cross sections along a plug for $Q_{aq} = Q_{IL} = 3.393$ ml/hr in 0.2 mm ID channel; Plane b is located at the center of the vortices; Planes a and c are at the beginning and end of the recirculation region, respectively. The velocity magnitude is superimposed in colour. The vectors represent the radial velocity.

$$\mathrm{fRe} = \underbrace{16}_{\text{Poiseuille flow}} + \underbrace{\frac{\alpha}{L^*}\left(\frac{\mathrm{Re}}{\mathrm{Ca}}\right)^{\beta}}_{\text{Interfacial}} \tag{8}$$

$$\frac{P}{L} = \varepsilon\left[f\left(\frac{1}{2}\rho U_{\mathrm{mix}2}\right)\frac{4}{D}\right] \tag{9}$$

where f is the Fanning friction factor, L*=Ls/D is the dimensionless length, Ls is the slug length, L is the capillary length, ε is the dispersed phase fraction, and α and β are fitting parameters. The friction factor calculated from the numerical simulations in both channels is plotted against $L^*(\mathrm{Ca}/\mathrm{Re})^{0.33}$ in Fig. 19. The inset illustrates the two limits of the single phase pressure drop and of the interfacial pressure drop as well as their sum over a wide range of conditions. Both asymptotes contribute significantly to the total pressure drop. The contribution of interfacial pressure drop can only be neglected for sufficiently long plugs. The best fit to the fRe data follows an order of −1 for $L^*(\mathrm{Ca}/\mathrm{Re})^{0.33}$, with a deviation of ±12.77%.

$$\mathrm{fRe} = 16 + \frac{0.225}{L^*}\left(\frac{\mathrm{Re}}{\mathrm{Ca}}\right)^{0.33} \tag{10}$$

The pressure drop per unit cell length, that includes a plug and a slug, from the CFD simulations is compared against Eq. (10) in Fig. 20 for both channels. The magnitude of the total pressure drop decreases significantly as the capillary size increases and the

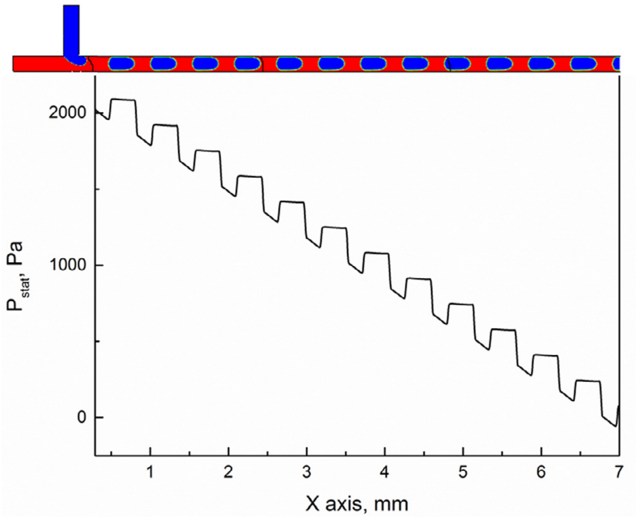

Fig. 17. Variation of pressure predicted by CFD along the channel for $Q_{aq} = Q_{IL} = 3.39$ ml/hr in the 0.2 mm ID channel.

difference becomes more significant at the higher mixture velocities. With increasing mixture velocity, the differences between the model and the simulations also increase with a maximum deviation of about 13.68% in the 0.2 mm channel. The differences arise mainly because of two reasons: 1) Eq. (10) was developed for gas-liquid flows and high Re ($150 < Re < 1400$; Kreutzer et al., 2005), but the Re in the present work falls between 0.049 and 1.229; 2) The experimental slug lengths used in Eq. (10), deviate more from the CFD predictions for short plugs (Section 2.2), and result in larger errors in the calculation of pressure drop at high mixture velocities.

More detailed approaches have also been developed to calculate the pressure drop in plug flow [12,23]. According to these models three contributions need to be taken into account. 1) Pressure drop in the continuous ionic liquid phase that can be described by the Hagen-Poiseuille law; 2) Pressure drop in the plug body where a uniform film thickness is assumed. The moving film pressure drop model by Fouilland et al. [64] will be used here (see Fig. 13); 3) Interfacial pressure drop at the front and rear ends of the plugs which depends on the interface curvature. These can be calculated following the model suggested by Bretherton [51] for drops of low viscosity compared to the continuous phase. The overall pressure drop per unit cell is given by Eq. (11):

$$\frac{\Delta P}{L} = \underbrace{\frac{8\mu_c U_{mix}}{R^2}\frac{L_s}{L}}_{}{}_{\text{Poiseuille flow}} + \underbrace{\frac{8\mu_c U_p}{R^2\left(1+\frac{R_p^4}{R^4}\right)\left(\frac{1}{\lambda}-1\right)}}_{}{}_{\text{Moving film}}\frac{L_{film}}{L} + \underbrace{\frac{C}{L}\frac{\gamma}{R}(3Ca)^{2/3}}_{}{}_{\text{Interfacial}} \tag{11}$$

The constant C is used to account for the interface curvature [23] and Marangoni effects [25]. It was found that $C = 1.03$ gives the smallest average deviation of 20.71% from the CFD predictions over the range of Ca numbers studied ($0.0224 < Ca < 0.299$). The deviations are smaller for the 0.5 mm channel where also plugs are longer. The non-uniform film thickness surrounding the short plugs and the rapid curvature change at the plug ends are responsible for the deviations.

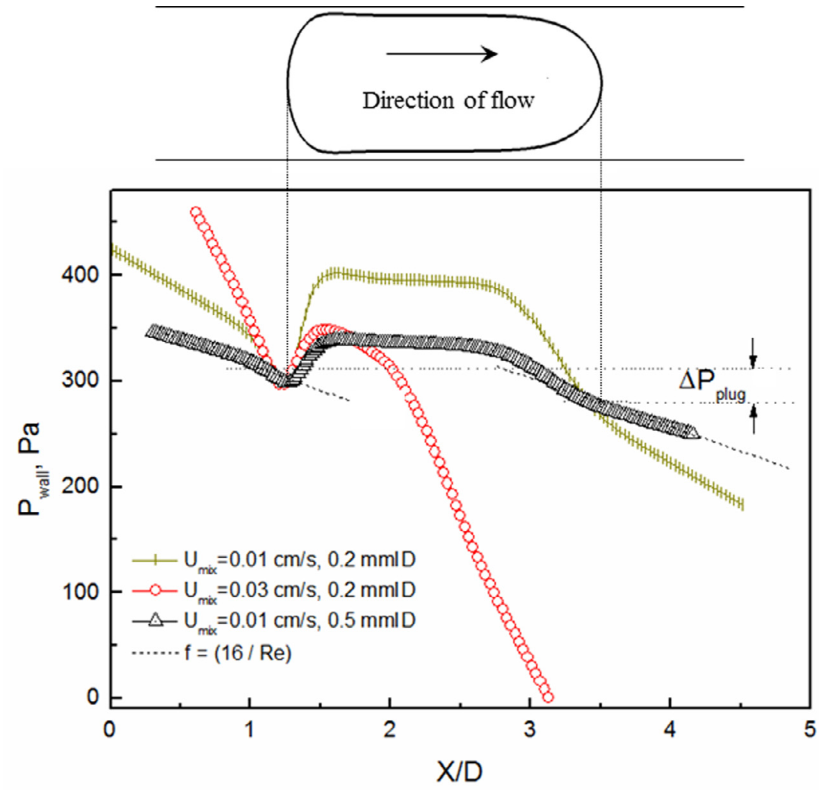

Fig. 18. Wall pressure distribution along a plug in the 0.2 mm and 0.5 mm ID channels. The dotted lines represent the projected pressure based on a linear regression of the pressure in the slug before and after the plug.

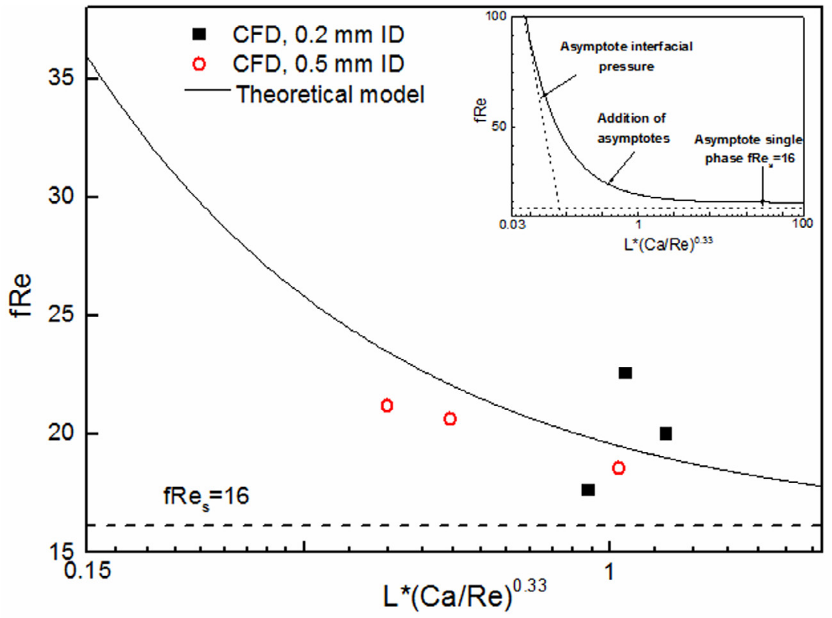

Fig. 19. Non-dimensional friction factor in the 0.2 mm and 0.5 mm ID channels for $Q_{aq} = Q_{IL}$ = 1.13–35.34 ml/hr. The inset shows the asymptotes for single phase and for interfacial pressure.

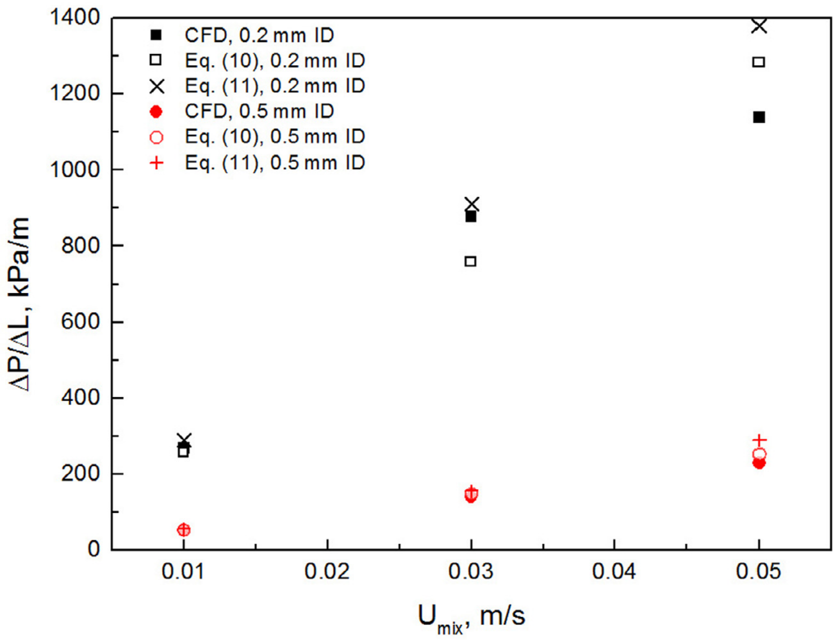

Fig. 20. Pressure gradient over a unit cell of a plug and a slug from CFD simulations (filled symbols) and the models given by Eqs. (10) and (11) (open symbols) in the 0.2 mm and 0.5 mm ID channels for $Q_{aq} = Q_{IL}$ = 1.131–35.34 ml/hr.

3. Conclusions

A systematic study of the hydrodynamics of liquid-liquid plug flow in 0.2 and 0.5 mm ID channels has been carried out using bright field micro-PIV and CFD modelling. The dispersed plug phase was 1 M HNO_3 aqueous solution while the continuous phase was a mixture of 0.2 M CMPO and 1.2 M TBP in an ionic liquid [C_4min][NTf_2]; this combination of liquids is used for enhanced Europium (III) recovery. It was found that the dimensionless film thickness is slightly smaller in the 0.2 mm channel than the 0.5 mm one under the same Ca. A correlation based on the one suggested by Mac Giolla Eain et al. [50] was proposed which predicts the film thickness within 0.27%–11.26% for Ca varying between 0.0224 and 0.299. The plug velocities in both channels were always higher than the mixture velocity, because of the nearly stagnant film surrounding the plugs. The plug length was found to be influenced by both the Capillary number and the flow rate ratio, which represent a balance of shear forces and Laplace pressure at the plug formation stage. The plug volume was highly dependent on the channel size and the mixture velocity.

Both the experimental and the computational velocity profiles showed that a parabolic profile forms in the middle of the plugs, while a Couette-shaped velocity profile develops in the surrounding continuous phase film. The recirculating flow patterns in the plugs were influenced by the flow velocities and the channel size. The pressure gradients predicted numerically agreed well with a correlation which included the dimensionless slug length and the ratio Ca/Re as parameters within 12.7%. These findings will help to optimise the properties of plug flow in microfluidic devices to improve mixing and enhance mass and heat mass transfer.

Acknowledgements

Financial support from the UCL Engineering Faculty and the China Scholarship Council is gratefully acknowledged. The authors would like to thank Prof. Kenneth R. Seddon and Dr. Natalia V. Plechkova of Queen's University Ionic Liquids Laboratories (QUILL) for providing the ionic liquids, and the UK Engineering and Physical Sciences Research Council (EPSRC) for the loan of the Photron Ultima APX high-speed camera.

References

[1] N. Assmann, A. Ładosz, P. Rudolf von Rohr, Continuous micro liquid-liquid extraction, Chem. Eng. Technol. 36 (2013) 921–936.

[2] B. Xu, W. Cai, X. Liu, X. Zhang, Mass transfer behavior of liquid–liquid slug flow in circular cross-section microchannel, Chem. Eng. Res. Des. 91 (2013) 1203–1211.

[3] L. Yang, Y. Zhao, Y. Su, G. Chen, An experimental study of copper extraction characteristics in a t-junction microchannel, Chem. Eng. Technol. 36 (2013) 985–992.

[4] J.R. Burns, C. Ramshaw, The intensification of rapid reactions in multiphase systems using slug flow in capillaries, Lab Chip 1 (2001) 10–15.

[5] J. Jovanović, E.V. Rebrov, T.A. Nijhuis, M.T. Kreutzer, V. Hessel, J.C. Schouten, Liquid-liquid flow in a capillary microreactor: hydrodynamic flow patterns and extraction performance, Ind. Eng. Chem. Res. 51 (2012) 1015–1026.

[6] Y. Okubo, T. Maki, N. Aoki, T. Hong Khoo, Y. Ohmukai, K. Mae, Liquid–liquid extraction for efficient synthesis and separation by utilizing micro spaces, Chem. Eng. Sci. 63 (2008) 4070–4077.

[7] M.N. Kashid, I. Gerlach, S. Goetz, J. Franzke, J.F. Acker, F. Platte, D.W. Agar, S. Turek, Internal circulation within the liquid slugs of a liquid−liquid slug-flow capillary microreactor, Ind. Eng. Chem. Res. 44 (2005) 5003–5010.

[8] J.G. Kralj, H.R. Sahoo, K.F. Jensen, Integrated continuous microfluidic liquid–liquid extraction, Lab Chip 7 (2007) 256–263.

[9] H. Breisig, M. Schmidt, H. Wolff, A. Jupke, M. Wessling, Droplet-based liquid–liquid extraction inside a porous capillary, Chem. Eng. J. 307 (2017) 143–149.

[10] Q. Li, P. Angeli, Intensified Eu(III) extraction using ionic liquids in small channels, Chem. Eng. Sci. 143 (2016) 276–286.

[11] W. Lan, S. Jing, X. Guo, S. Li, Study on "interface – shrinkage – driven" breakup of droplets in co-flowing microfluidic devices, Chem. Eng. Sci. 158 (2017) 58–63.

[12] R. Gupta, S.S.Y. Leung, R. Manica, D.F. Fletcher, B.S. Haynes, Hydrodynamics of liquid–liquid Taylor flow in microchannels, Chem. Eng. Sci. 92 (2013) 180–189.

[13] Y. Han, N. Shikazono, Measurement of the liquid film thickness in micro tube slug flow, Int. J. Heat Fluid Flow 30 (2009) 842–853.

[14] A.-L. Dessimoz, L. Cavin, A. Renken, L. Kiwi-Minsker, Liquid–liquid two-phase flow patterns and mass transfer characteristics in rectangular glass microreactors, Chem. Eng. Sci. 63 (2008) 4035–4044.

[15] H. Foroughi, M. Kawaji, Viscous oil–water flows in a microchannel initially saturated with oil: Flow patterns and pressure drop characteristics, Int. J. Multiph. Flow 37 (2011) 1147–1155.

[16] M.N. Kashid, W. Kowaliński, A. Renken, J. Baldyga, L. Kiwi-Minsker, Analytical method to predict two-phase flow pattern in horizontal micro-capillaries, Chem. Eng. Sci. 74 (2012) 219–232.

[17] P. Angeli, A. Gavriilidis, Hydrodynamics of Taylor flow in small channels: a review, in: Proceedings of the Institution of Mechanical Engineers, Part C: Journal of Mechanical Engineering Science, 222 (2008) 737-751.

[18] P. Garstecki, M.J. Fuerstman, H.A. Stone, G.M. Whitesides, Formation of droplets and bubbles in a microfluidic T-junction-scaling and mechanism of break-up, Lab Chip 6 (2006) 437–446.

[19] S. Van der Graaf, T. Nisisako, C.G.P.H. Schroën, R.G.M. van der Sman, R.M. Boom, Lattice boltzmann simulations of droplet formation in a T-shaped microchannel, Langmuir 22 (2006) 4144–4152.

[20] J.H. Xu, S.W. Li, J. Tan, G.S. Luo, Correlations of droplet formation in T-junction microfluidic devices: from squeezing to dripping, Microfluid. Nanofluid. 5 (2008) 711–717.

[21] T. Fu, Y. Ma, D. Funfschilling, C. Zhu, H.Z. Li, Squeezing-to-dripping transition for bubble formation in a microfluidic T-junction, Chem. Eng. Sci. 65 (2010) 3739–3748.

[22] D. Tsaoulidis, P. Angeli, Effect of channel size on liquid-liquid plug flow in small channels, AIChE J. 62 (2016) 315–324.

[23] J. Jovanović, W. Zhou, E.V. Rebrov, T. Nijhuis, V. Hessel, J.C. Schouten, Liquid–liquid slug flow: hydrodynamics and pressure drop, Chem. Eng. Sci. 66 (2011) 42–54.

[24] E. Walsh, Y. Muzychka, P. Walsh, V. Egan, J. Punch, Pressure drop in two phase slug/bubble flows in mini scale capillaries, Int. J. Multiph. Flow 35 (2009) 879–884.

[25] M.T. Kreutzer, F. Kapteijn, J.A. Moulijn, C.R. Kleijn, J.J. Heiszwolf, Inertial and interfacial effects on pressure drop of Taylor flow in capillaries, AIChE J. 51 (2005) 2428–2440.

[26] E.D. Walker, Numerical Studies of Liquid-Liquid Segmented Flows in Square Microchannels Using a Front-Tracking Algorithm, in, PhD thesis. Louisiana State University, 2016.

[27] X.-B. Li, F.-C. Li, J.-C. Yang, H. Kinoshita, M. Oishi, M. Oshima, Study on the mechanism of droplet formation in T-junction microchannel, Chem. Eng. Sci. 69 (2012) 340–351.

[28] H. Liu, Y. Zhang, Droplet formation in a T-shaped microfluidic junction, J. Appl. Phys. 106 (2009) 034906.

[29] S. Afkhami, A. Leshansky, Y. Renardy, Numerical investigation of elongated drops in a microfluidic T-junction, Physics of Fluids (1994-present), 23 (2011) 022002.

[30] Y. Yan, D. Guo, S.Z. Wen, Numerical simulation of junction point pressure during droplet formation in a microfluidic T-junction, Chem. Eng. Sci. 84 (2012) 591–601.

[31] V. Talimi, Y.S. Muzychka, S. Kocabiyik, A review on numerical studies of slug flow hydrodynamics and heat transfer in microtubes and microchannels, Int. J. Multiph. Flow 39 (2012) 88–104.

[32] G. Kurup, A.S. Basu, Shape dependent Laplace vortices in deformed liquid-liquid slug flow, in: 2011 Annual International Conference of the IEEE Engineering in Medicine and Biology Society, IEEE, 2011, pp. 4034-4037.

[33] S. Kececi, M. Wörner, A. Onea, H.S. Soyhan, Recirculation time and liquid slug mass transfer in co-current upward and downward Taylor flow, Catal. Today 147 (Supplement) (2009) S125–S131.

[34] T. Abadie, C. Xuereb, D. Legendre, J. Aubin, Mixing and recirculation characteristics of gas–liquid Taylor flow in microreactors, Chem. Eng. Res. Des. 91 (2013) 2225–2234.

[35] M. Chinaud, E.-P. Roumpea, P. Angeli, Studies of plug formation in microchannel liquid–liquid flows using advanced particle image velocimetry techniques, Exp. Thermal Fluid Sci. 69 (2015) 99–110.

[36] V. Dore, D. Tsaoulidis, P. Angeli, Mixing patterns in water plugs during water/ionic liquid segmented flow in microchannels, Chem. Eng. Sci. 80 (2012) 334–341.

[37] H. Kinoshita, S. Kaneda, T. Fujii, M. Oshima, Three-dimensional measurement and visualization of internal flow of a moving droplet using confocal micro-PIV, Lab Chip 7 (2007) 338–346.

[38] D. Tsaoulidis, V. Dore, P. Angeli, N.V. Plechkova, K.R. Seddon, Dioxouranium(VI) extraction in microchannels using ionic liquids, Chem. Eng. J. 227 (2013) 151–157.

[39] A. Rout, K.A. Venkatesan, T.G. Srinivasan, P.R. Vasudeva, Rao, Room temperature ionic liquid diluent for the extraction of Eu(III) using TRUEX extractants, J. Radioanal. Nucl. Chem. 290 (2011) 215–219.

[40] C. Meinhart, S. Wereley, M. Gray, Volume illumination for two-dimensional particle image velocimetry, Meas. Sci. Technol. 11 (2000) 809.

[41] S.M. Hagsäter, C.H. Westergaard, H. Bruus, J.P. Kutter, Investigations on LED illumination for micro-PIV including a novel front-lit configuration, Exp. Fluids 44 (2007) 211–219.

[42] C.D. Meinhart, S.T. Wereley, J.G. Santiago, PIV measurements of a microchannel flow, Exp. Fluids 27 (1999) 414–419.

[43] J. Meadows, A.K. Agrawal, Time-resolved PIV of lean premixed combustion without and with porous inert media for acoustic control, Combust. Flame 162 (2015) 1063–1077.

[44] L.S. Han, Hydrodynamic Entrance Lengths for Incompressible Laminar Flow in Rectangular Ducts, J. Appl. Mech. 27 (1960) 403–409.

[45] N. Dombrowski, E.A. Foumeny, S. Ookawara, A. Riza, The influence of reynolds number on the entry length and pressure drop for laminar pipe flow, Can. J. Chem. Eng. 71 (1993) 472–476.

[46] D. Lakehal, G. Larrignon, C. Narayanan, Computational heat transfer and two-phase flow topology in miniature tubes, Microfluid. Nanofluid. 4 (2008) 261–271.

[47] R. Navaneetha Krishnan, S. Vivek, D. Chatterjee, S.K. Das, Performance of numerical schemes in the simulation of two-phase free flows and wall bounded mini channel flows, Chem. Eng. Sci. 65 (2010) 5117–5136.

[48] C. Fang, C. Hidrovo, F.-M. Wang, J. Eaton, K. Goodson, 3-D numerical simulation of contact angle hysteresis for microscale two phase flow, Int. J. Multiph. Flow 34 (2008) 690–705.

[49] Y. Li, R.K. Reddy, C.S.S.R. Kumar, K. Nandakumar, Computational investigations of the mixing performance inside liquid slugs generated by a microfluidic T-junction, Biomicrofluidics 8 (2014) 054125.

[50] M. Mac, Giolla Eain, V. Egan, J. Punch, Film thickness measurements in liquid–liquid slug flow regimes, Int. J. Heat Fluid Flow 44 (2013) 515–523.

[51] F.P. Bretherton, The motion of long bubbles in tubes, J. Fluid Mech. 10 (1961) 166–188.

[52] S. Irandoust, B. Andersson, Liquid film in Taylor flow through a capillary, Ind. Eng. Chem. Res. 28 (1989) 1684–1688.

[53] P. Aussillous, D. Quéré, Quick deposition of a fluid on the wall of a tube, Phys. Fluids 12 (2000) 2367–2371.

[54] D.R. Langewisch, J. Buongiorno, Prediction of film thickness, bubble velocity, and pressure drop for capillary slug flow using a CFD-generated database, Int. J. Heat Fluid Flow 54 (2015) 250–257.
[55] H. Liu, C.O. Vandu, R. Krishna, Hydrodynamics of taylor flow in vertical capillaries: flow regimes bubble rise velocity, liquid slug length, and pressure drop, Indus. Eng. Chem. Res. 44 (2005) 4884–4897.
[56] C.D. Meinhart, S.T. Wereley, J.G. Santiago, A PIV algorithm for estimating time-averaged velocity fields, J. Fluids Eng. 122 (2000) 285–289.
[57] G.F. Christopher, N.N. Noharuddin, J.A. Taylor, S.L. Anna, Experimental observations of the squeezing-to-dripping transition in T-shaped microfluidic junctions, Phys. Rev. E 78 (2008) 036317.
[58] T. Fu, Y. Wu, Y. Ma, H.Z. Li, Droplet formation and breakup dynamics in microfluidic flow-focusing devices: From dripping to jetting, Chem. Eng. Sci. 84 (2012) 207–217.
[59] S. Laborie, C. Cabassud, L. Durand-Bourlier, J.M. Lainé, Characterisation of gas–liquid two-phase flow inside capillaries, Chem. Eng. Sci. 54 (1999) 5723–5735.
[60] D. Qian, A. Lawal, Numerical study on gas and liquid slugs for Taylor flow in a T-junction microchannel, Chem. Eng. Sci. 61 (2006) 7609–7625.
[61] P. Sobieszuk, P. Cygański, R. Pohorecki, Bubble lengths in the gas–liquid Taylor flow in microchannels, Chem. Eng. Res. Des. 88 (2010) 263–269.
[62] T.A. Prileszky, B.A. Ogunnaike, E.M. Furst, Statistics of droplet sizes generated by a microfluidic device, AIChE J. 62 (2016) 2923–2928.
[63] E. Lac, J. Sherwood, Motion of a drop along the centreline of a capillary in a pressure-driven flow, J. Fluid Mech. 640 (2009) 27–54.
[64] T.S. Fouilland, D.F. Fletcher, B.S. Haynes, Film and slug behaviour in intermittent slug–annular microchannel flows, Chem. Eng. Sci. 65 (2010) 5344–5355.
[65] T.C. Thulasidas, M.A. Abraham, R.L. Cerro, Flow patterns in liquid slugs during bubble-train flow inside capillaries, Chem. Eng. Sci. 52 (1997) 2947–2962.
[66] C.N. Baroud, F. Gallaire, R. Dangla, Dynamics of microfluidic droplets, Lab Chip 10 (2010) 2032–2045.
[67] S. Hodges, O. Jensen, J. Rallison, The motion of a viscous drop through a cylindrical tube, J. Fluid Mech. 501 (2004) 279–301.
[68] T. Abadie, J. Aubin, D. Legendre, On the combined effects of surface tension force calculation and interface advection on spurious currents within Volume of Fluid and Level Set frameworks, J. Comput. Phys. 297 (2015) 611–636.
[69] C. Meyer, M. Hoffmann, M. Schlüter, Micro-PIV analysis of gas–liquid Taylor flow in a vertical oriented square shaped fluidic channel, Int. J. Multiph. Flow 67 (2014) 140–148.